

# Decoupled Trace Element and Isotope Compositions Recorded in Orthopyroxene and Clinopyroxene in Composite Pyroxenite Veins from the Xiugugabu Ophiolite (SW Tibet)

Zhen-Yu Zhang<sup>1,3,4</sup>, Chuan-Zhou Liu<sup>1,2,3,\*</sup>, Yan Liang<sup>4,\*</sup>, Chang Zhang<sup>1</sup>, Tong Liu<sup>1</sup>, Wei-Qi Zhang<sup>1</sup> and Wen-Bin Ji<sup>5</sup>

<sup>1</sup>State Key Laboratory of Lithospheric Evolution, Institute of Geology and Geophysics, Chinese Academy of Sciences, Beijing 100029, China

<sup>2</sup>Laboratory for Marine Geology, Qingdao National Laboratory for Marine Science and Technology, Qingdao 266061, China

<sup>3</sup>College of Earth and Planetary Sciences, University of Chinese Academy of Sciences, Beijing 100049, China

<sup>4</sup>Department of Earth, Environmental and Planetary Sciences, Brown University, Providence, RI 02912, USA

<sup>5</sup>Department of Geology, Northwest University, Xi'an, Shaanxi Province 710069, China

\*Corresponding author. E-mail: chzliu@mail.iggcas.ac.cn, yan\_liang@brown.edu

## Abstract

Pyroxenite veins and dikes are commonly observed in the mantle section of ophiolites. Because of their mantle occurrence, these pyroxenites are free from crustal contamination and offer a unique opportunity for studying mantle compositions and melt–rock interaction processes. We conducted an integrated petrological and geochemical study of a suite of composite orthopyroxenite, websterite, and pyroxene-bearing dunite veins from the Xiugugabu ophiolite located on the western segment of Yarlung–Zangbo Suture Zone. The dunite is separated from the host peridotite by a layer of pyroxenite, forming a composite vein system. Systematic variations in major, minor, and trace element compositions in minerals across the composite veins are observed. Two generations of orthopyroxenes in the pyroxenites are characterized by high Mg#, low TiO<sub>2</sub> concentrations, and depleted patterns of incompatible trace elements. Clinopyroxenes in the pyroxenites are characterized by high Mg#, low contents of TiO<sub>2</sub> and Na<sub>2</sub>O, spooned shaped REE patterns, and a negative Zr anomaly. Through major and trace element modeling, we showed that both orthopyroxene and clinopyroxene were in equilibrium with melts with different compositions. This hypothesis is further confirmed by distinct initial Nd and Hf isotope ratios in the two pyroxenes. A model for the formation of composite pyroxenite veins is developed, whereby hydrous and silica-rich melts percolate along the margins of a dunite channel. The orthopyroxenite was formed by the reaction between a hydrous, silica-rich melt and the surrounding peridotite. The websterite is formed by reactive crystallization of a hybrid melt produced by mixing silica-rich melt and the melt formed by remelting of previously depleted peridotite in the deeper part of the mantle column. The extremely enriched Nd–Hf isotope compositions of the pyroxenite veins ( $\epsilon_{\text{Nd}} = -20.3$  to  $+11.5$  and  $\epsilon_{\text{Hf}} = -13.2$  to  $+25.3$ , 125 million years ago) can be explained by the addition of ancient, recycled sediments to the mantle source in a supra-subduction setting. Based on the low-Cr# spinel in the Xiugugabu dunites (Cr# = 19–50) and the depleted nature of the parental melt of the Xiugugabu pyroxenites, we deduced that the formation of pyroxenites postdate the formation of the Xiugugabu ophiolite at ~125–130 Ma. Collectively, results from this study have provided support to the hypothesis that the Xiugugabu ophiolite experience a two-stage evolution, i.e., firstly formed in a mid-ocean ridge setting and subsequently modified in a supra subduction zone.

**Keywords:** mantle heterogeneity, Tibet Plateau, Xiugugabu ophiolite, Nd–Hf isotope, pyroxenites

## INTRODUCTION

Although volumetrically minor, pyroxenite veins and dikes are commonly observed in abyssal peridotites (Dantas *et al.*, 2007; Laukert *et al.*, 2014; Warren *et al.*, 2009), orogenic peridotites (Bodinier *et al.*, 1987; Garrido & Bodinier, 1999; Downes, 2007; Gysi *et al.*, 2011; Xiong *et al.*, 2014), and ophiolitic peridotites (Python & Ceuleneer, 2003; Tamura & Arai, 2006; Borghini *et al.*, 2013; Le Roux & Liang, 2019; Belousov *et al.*, 2021). Fragments of pyroxenite and pyroxenite–peridotite composite are also observed as mantle xenoliths from a variety of continental settings (Frey & Prinz, 1978; Chen & Zhou, 2005;

Liu *et al.*, 2005; Dantas *et al.*, 2009; Ionov *et al.*, 2018). The lithology and origin of pyroxenite is diverse, including orthopyroxenite, websterite, and clinopyroxenite, some of which contain hydrous minerals such as amphibole.

Three mechanisms have been proposed for the formation of pyroxenite in mantle peridotites: they represent (1) metamorphosed recycled oceanic crust that was stretched in the asthenosphere by mantle convection and eventually incorporated into lithospheric mantle (Allègre & Turcotte, 1986; Morishita *et al.*, 2003; Yu *et al.*, 2010), (2) cumulates of percolating melts derived from the asthenosphere (Dantas *et al.*, 2007;

Warren *et al.*, 2009; Seyler *et al.*, 2011; Xiong *et al.*, 2014), or (3) products of reaction between through-going melts and host peridotites (Garrido & Bodinier, 1999; Bodinier *et al.*, 2008; Borghini *et al.*, 2016; Tilhac *et al.*, 2016). Based on structural and textural relationships with the host peridotite, Bodinier & Godard (2014) subdivided pyroxenites into three groups: (1) dikes and veins showing a clear crosscutting boundary with the peridotite foliation and compositional layering, which are crystallized from deep-seated melt and hence not genetically related to the host peridotites; (2) replacive pyroxenites occurring as straight layers parallel to the foliation of host peridotite, which are formed by melt-peridotite reaction at conditions close to the solidus of peridotite; and (3) deformed pyroxenites occurring as isoclinally folded and boudinaged layers or patches in host peridotites, some of which represent recycled materials due to their chemical similarity to the oceanic crust (e.g., a positive 'europium' anomaly in a formerly plagioclase-bearing lithology, a depleted heavy rare earth element (REE) garnet signature, and  $\delta^{18}\text{O}$  values as low as 4.5‰).

The present study focuses on pyroxenite veins from the Xiugugabu ophiolite, which is located on the western segment of the Yarlung–Zangbo Suture Zone (YZSZ). Previous studies have been conducted on the structural, petrological, and geochemical features of the mantle peridotites and the mafic dikes intruding into the mantle peridotites in the south part of the Xiugugabu ophiolite (Bezard *et al.*, 2011; Zhong *et al.*, 2019). While pyroxenites and dunites are frequently found intruding into the mantle peridotite in the Xiugugabu ophiolite, no cross-cutting relationships between mafic dikes and ultramafic pyroxenitic veins have been found in the Xiugugabu ophiolite. Here, we present, for the first time, detailed petrological observations, elemental concentrations, and Nd–Hf isotopes of the Xiugugabu pyroxenites and pyroxene-bearing dunite, which enable us to systematically investigate magmatic processes leading to the formation of these pyroxenite veins and the nature of their mantle sources. A two-stage model is proposed to interpret the possible tectonic settings from which the Xiugugabu ophiolite was originated. The Xiugugabu ophiolite formed in a mid-ocean ridge (MOR) and subsequently experienced a subduction re-initiation process.

## GEOLOGICAL BACKGROUND AND SAMPLE DESCRIPTION

### Geological background

The Tibetan Plateau is an orogenic collage formed by the northward accretion of a series of terranes, which are separated by three well-defined suture zones (Yin & Harrison, 2000), i.e., the Jinsha River Suture Zone, the Bangong–Nujiang Suture Zone, and the YZSZ (Fig. 1a). The nearly W–E trending YZSZ marks the final closure of Neo-Tethys Ocean, which separates the Lhasa block to the north from the Indian plate to the south.

Geological units neighboring the YZSZ, from north to south, include the Gangdese batholith, the Xigaze forearc basin, the Yarlung–Zangbo ophiolites, accretionary mélange, and Tethyan Himalayan strata (Fig. 1b). The Gangdese batholith was generated during subduction of the Neo-Tethys Ocean during the Jurassic or earlier (Chung *et al.*, 2005; Ji *et al.*, 2009; Ji *et al.*, 2014; Wang *et al.*, 2016a). Sedimentary strata deposited in the Xigaze forearc basin, from the bottom up, include radiolarian chert, deep- to shallow-water turbidites, and clastic rocks (Wu *et al.*, 2010; An *et al.*, 2014; Wang *et al.*, 2017). Zircon U–Pb dating on the tuff layers interlayered within the radiolarian cherts suggests that deposition in the Xigaze forearc basin was no earlier than ~119 Ma (Wang *et al.*, 2017). To the south of the forearc basin, the YZSZ ophiolites are exposed, and previous geochronological studies on ocean crustal rocks (i.e., gabbros, diabases, and plagiogranites) have yielded Early Cretaceous ages of ~119–132 Ma (Guilmette *et al.*, 2009; Dai *et al.*, 2013; Liu *et al.*, 2016b; Zhang *et al.*, 2016a; Cheng *et al.*, 2018; Zhong *et al.*, 2019). The Tethyan Himalayan sequences are Permian to Cretaceous sedimentary rocks that were deposited on the Indian passive continental margin (Liu & Einsele, 1996; Liu & Einsele, 1999; Yang *et al.*, 2005; Guangwei *et al.*, 2010).

The YZSZ is geographically subdivided into three segments: the eastern (Luobusa–Zedang), central (Renbu–Sangsang), and western (Saga to Dongbo) segments (Fig. 1a). In general, the YZSZ has a coherent ophiolitic sequence consisting of a thick mantle section (>7 km thick) and a thin crustal section (<3 km) (e.g., Nicolas *et al.*, 1981; Girardeau *et al.*, 1985; Liu *et al.*, 2021), which is typical of present-day slow-spreading ridges (Dick *et al.*, 2003; Cannat *et al.*, 2006). Along the YZSZ, the mafic crustal rocks are geochemically similar to MOR basalts (MORBs) (e.g., Liu *et al.*, 2016; Zhang *et al.*, 2016b) and mantle peridotites geochemically resemble global peridotites (e.g., Liu *et al.*, 2014, 2019; Warren, 2016; Zhang *et al.*, 2020a, 2020b), which are indicative of mid-ocean setting. However, mafic crustal rocks intruding into mantle peridotites of the YZSZ show enrichment in large ion lithophile elements (LILEs; e.g., Li, K, Rb, and Cs) and depletion in high-field-strength elements (HFSEs; e.g., Nb, Ta, Zr, and Hf) (e.g., Bezard *et al.*, 2011; Dai *et al.*, 2013, 2021; Xiong *et al.*, 2016, 2017b; Zhong *et al.*, 2019), suggesting a supra-subduction zone (SSZ) setting.

The Xiugugabu ophiolite, located at the western segment of the YZSZ, is a ~260-km<sup>2</sup> fragment of oceanic lithosphere lying on the Cretaceous tectonic mélange. It mainly consists of mantle rocks (Fig. 1c). A diabase unit, which is geochemically similar to oceanic island basalt (OIB), occurs in the NE flank of the ophiolite (Bezard *et al.*, 2011). The latter is overlain by a Triassic sedimentary sequence (Xiukang Strata; Fig. 1c). The mantle rocks are mainly composed of lherzolites and clinopyroxene-bearing harzburgites. Dunites locally occur as irregular pockets or veinlets within the lherzolites and clinopyroxene-bearing harzburgites. In the

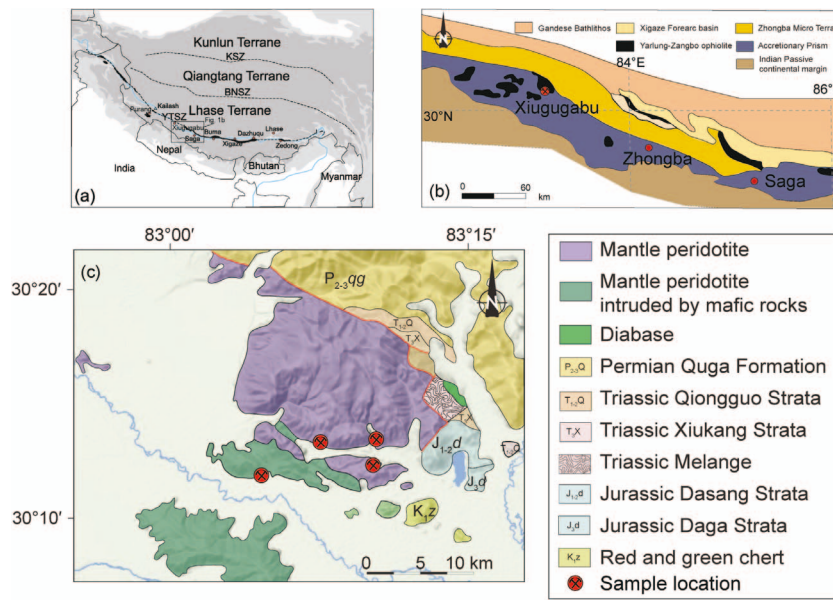


**Fig. 1.** (a) Simplified tectonic map of the Tibetan Plateau showing several main suture zones; (b) geological sketch map of western segment of the YZSZ illustrating the location of the Xiuqigabu ophiolite; (c) geological map of the Xiuqigabu ophiolite with the sample locations. Note mantle section is in fault contact with the Permian to Jurassic strata.

south flank of the ophiolite, mantle peridotites are commonly intruded by diabase/gabbroic dikes and sills, which have been dated by multiple geochronological methods:  $126.2 \pm 9.1$  Ma (Sm–Nd; Xu *et al.*, 2008);  $120.3 \pm 3.1$  to  $122.3 \pm 2.4$  Ma (zircon U–Pb; Zhong *et al.*, 2019, and Wei *et al.*, 2006, respectively). These mafic intrusions have geochemical affinity of MORB, but with variable degrees of contamination by crustal materials in their mantle source (Xu *et al.*, 2008; Bezard *et al.*, 2011; Zhong *et al.*, 2019). In addition, veinlets of orthopyroxenites, websterites, and gabbronorites occur within mantle peridotites (Fig. 2).

### Sample description and modal compositions

Pyroxenites hosted in the Xiuqigabu dunites or harzburgites mostly occur as swarms of subparallel veins (Fig. 2a) or elongated lenses/patches (Fig. 2b). The width of pyroxenite veins ranges from thin and diffusive pyroxene layers (<1 cm) to thick pyroxenites (~10 cm). The pyroxenite veins are lithologically symmetric on either side of dunite hosted by harzburgites (Fig. 2a). The boundary or interface between pyroxenites and their surrounding dunites and/or harzburgites is relatively sharp and can be easily identified (Fig. 2; Appendix 1). Websterite veins are more abundant than orthopyroxenite veins. Eight samples, including one composite dunite-orthopyroxenite-websterite vein, five olivine websterites, one plagioclase-bearing orthopyroxenite, and one pyroxene-bearing dunite, were selected for study. Their host peridotites are also studied for comparison. Images of pyroxenite veins included in this study are presented in Figs 3 and 4; Appendix 1. Mineral modes were obtained by counting 3000–3500 points for each thin section using the image analyzing program, JmicroVision (Roudit, 2008). Mineral modes

of five samples were also obtained through mass-balance calculation using their bulk-rock and mineral major element concentrations. The weight proportions were converted to volume proportions assuming the following density ratios: clinopyroxene/olivine = 1.03, orthopyroxene/olivine = 0.97, and spinel/olivine = 1.1 (Le Roux *et al.*, 2014). The calculated modal contents are given in Table 1. Two samples (17TP18-2 and 17TP21) show good agreements between the two methods. The composite pyroxenite veins 17TP19 and the olivine websterite 17TP22 have much higher calculated olivine modes, while olivine websterite 17TP25 has a higher calculated orthopyroxene mode. This is likely due to the small size of the thin section that might not capture the distribution of pyroxenite veins in the host rock. Hereafter, we will use point-counted modes to classify pyroxenites and mass-balance modes to reconstruct their bulk rock trace element concentrations.

### Composite dunite–orthopyroxenite–websterite and olivine websterite veins

Sample 17TP19 is a typical composite vein consisting of dunite, orthopyroxenite, and websterite from center to edge (Fig. 3a and b). Within the dunite part, coarse-to fine-grained olivines show kink bands and undulose extinction. Spinels are subhedral to anhedral and aligned along the vein, with a maximum grain size of ~1 mm (Fig. 3c). Spinels in the dunite are coarser than those in the surrounding pyroxenite and harzburgite (Fig. 3a; Appendix 1). Separated from the dunite by a diffuse boundary, the orthopyroxenite vein mainly consists of porphyroclastic orthopyroxene ( $Wo_1En_{89}Fs_{10}$ ; Fig. 3a and b). The websterites (17TP19-1 and 17TP 19-5) are mainly composed of porphyroclastic orthopyroxene ( $Wo_{1-3}En_{87-9}Fs_{10-11}$ ) in a fine-grained matrix



**Fig. 2.** Photograph of the outcrop showing spatial relations of the Xiugugabu pyroxenites and their host peridotites. (a) Composite dunite–websterite–harzburgite veins. Foliation in the host peridotites is defined by the elongated pyroxene-bearing and pyroxene-poor bands. (b) Highly deformed pyroxenite veins/patches and associated dunites and harzburgites. (c) Websterite veins parallel to the foliation of reactive harzburgites; (d) gabbronorite vein cross-cut websterite veins and surrounding peridotites.

**Table 1:** Texture, modal composition, and equilibrated temperature of the Xiugugabu pyroxenite veins and pyroxene-bearing dunite

Sam- ple	Lithol- ogy	Tex- ture	Mode				T(°C)		
			Ol	Opx	Cpx	Sp	T <sub>BKN</sub>	T <sub>Ca</sub>	T <sub>REE</sub>
17TP18-1	Ol-websterite	Porphyroclastic	18.3	69.2	10.4	2.1	868	1045	1214
17TP18-2	Ol-websterite	Equigranular/porphyroclastic	17.8 (22.1)	67.2 (62.3)	13.0 (14.8)	2.0 (0.8)	790	939	1027
17TP19	19-1 Websterite	Equigranular/porphyroclastic	2.4	59.2	37.8	0.6	882	1044	1046
	19-3 Ol-orthopyroxenite	Porphyroclastic	8 (35.4)	89.8 (54.5)	1.6 (7.5)	0.6 (2.7)	761	884	—
	19-5 Ol-websterite	Equigranular/porphyroclastic	5.4	64.2	28.8	1.6	860	977	1140
17TP21	Pyroxene-bearing dunite	Equigranular	56.8 (59.0)	27.4 (26.1)	13.4 (10.7)	2.4 (3.6)	975	1060	1044
17TP22	Ol-websterite	Equigranular	12.9 (64.5)	68.6 (30.4)	15.9 (5.1)	2.6 (0.0)	805	1016	1073
17TP25	Ol-websterite	Equigranular/porphyroclastic	7.6 (7.3)	32.4 (50.8)	58.4 (40.3)	1.6 (0.4)	830	951	1144
17TP29	Pl-orthopyroxenite	Porphyroclastic	1.6	95.7	2.3	0.4	750	901	—
17TP30	Ol-websterite	Equigranular/porphyroclastic	17.2	59.4	22.8	0.6	808	882	1193

The mineral modal contents have been estimated by point-counting and mass-balance calculation between whole rock and mineral chemistry. The results from mass-balance calculation were presented in parentheses. The sample 17TP21 is the pyroxene-bearing dunite rather a lherzolite (see Appendix 1). Ol indicates olivine; Sp, spinel; Cpx, clinopyroxene; Opx, orthopyroxene.

of orthopyroxene ( $Wo_{1-2}En_{88-89}Fs_{10-11}$ ) and clinopyroxene ( $Wo_{47-50}En_{4-5}Fs_{45-49}$ ) neoblasts (Fig. 3c and d; Appendix 1). From the dunite-orthopyroxenite contact to the websterite-harzburgite contact, the modal abundance of vermicular spinels decreases, whereas the modal abundance of clinopyroxene increases (cf. Fig. 3a and b).

The five olivine websterites included in this study are hosted in dunite. Except for the olivine websterite 17TP25, orthopyroxene is the most abundant mineral in olivine websterites (32–69 vol.%; Table 1). All the olivine websterites display a porphyroclastic texture (Fig. 4d–g; Appendix 1) with orthopyroxene as porphyroclasts (grain size up to 1.1 cm; Appendix 1). The porphyroclastic orthopyroxene often encloses olivine poikiloblasts (Fig. 4a). The matrix is fine-grained (0.1–0.5 mm)

and consists of clinopyroxene and orthopyroxene neoblasts (Fig. 4c). Interestingly, some coarse orthopyroxene

porphyroclasts (>500  $\mu\text{m}$ , orthopyroxene 1) have a similar grain size as orthopyroxene in the host harzburgite and exhibit extensive clinopyroxene exsolution (clinopyroxene blobs in Fig. 4e and f), whereas other orthopyroxene porphyroclasts and clinopyroxene and orthopyroxene neoblasts (<500  $\mu\text{m}$ , orthopyroxene 2, and clinopyroxene 2) display no or narrow exsolution lamellae. Olivine and spinel are present as small idiomorphic interstitial grains along the pyroxene grain boundaries or junctions (Fig. 4c). The vermicular relic grains of olivine display kink bands and undulose extinctions similar to olivines in their host rock (Appendix 1) and are partly replaced by orthopyroxene (Fig. 4c).

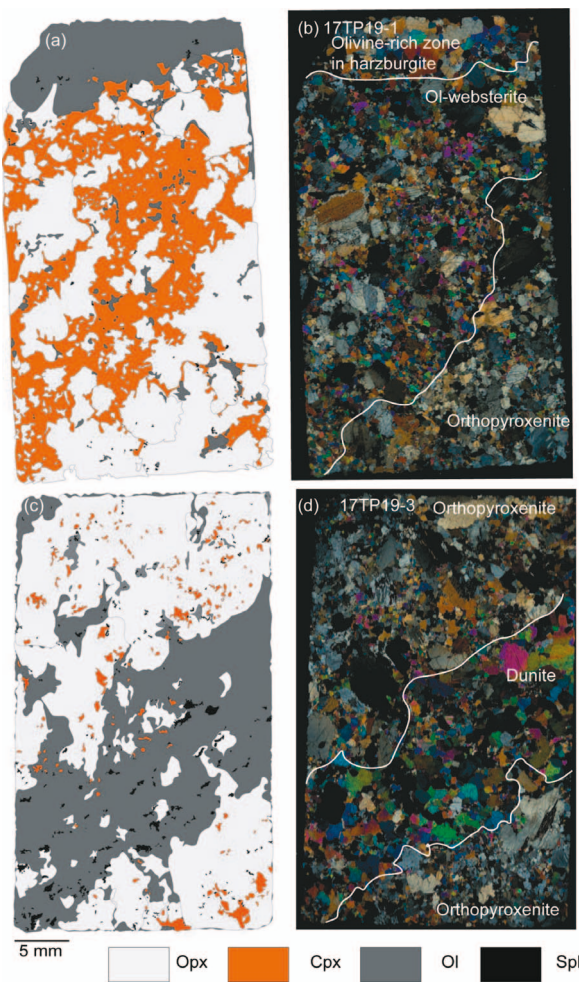


**Fig. 3.** Sketches (a, c) and crossed polarized images (b, d) of typical thin sections from the composite dunite-orthopyroxenite-websterite vein 17TP19. Note the orthopyroxene porphyroclasts in the websterite and orthopyroxenite (a, c) and small orthopyroxene grains and trails of spinel in the dunite (c). The sketches were drawn mainly based on BSE images. Abbreviations: Ol, olivine; Sp, spinel; Cpx, clinopyroxene; Opx, orthopyroxene.

Anhedral spinels are often associated with olivine, whereas euhedral poikilitic spinels are enclosed in pyroxenes on rare occasions (Fig. 4c).

The olivine websterite 17TP25 is distinct due to its higher proportion of clinopyroxene than orthopyroxene (58 vol.% vs 32 vol.%, respectively; Table 1; Appendix 1). A small elongated dunite vein is enclosed in the websterite vein (Appendix 1). Rare interstitial amphiboles grains (<0.2 mm) are found along the boundaries between clinopyroxene and orthopyroxene.

#### Plagioclase-bearing orthopyroxenite (17TP29)

In addition to orthopyroxene (~96 vol.%), the orthopyroxenite (17TP29) contains small amount of olivine (1.6 vol.%), clinopyroxene (2.3 vol.%), spinel (0.4 vol.%), and a very small amount of plagioclase. The porphyroclastic orthopyroxene has a grain size of up to 5 mm (Appendix 1) and olivine-orthopyroxene-spinel-plagioclase assemblages can be found interstitially along

the boundaries of irregularly shaped orthopyroxene grains (Fig. 4i).

#### Pyroxene-bearing dunites

The dunite sample 17TP21 contains a ~3-cm spinel- and pyroxene-bearing vein (Appendix 1), which consists of 61% olivine, 25% orthopyroxene, 12% clinopyroxene, and 2% spinel. The boundary between the dunite and pyroxene-bearing vein is not sharp. Both orthopyroxene and clinopyroxene have comparable grain sizes and show interfingering textures. We regard orthopyroxene-clinopyroxene aggregates as micro-pyroxenites within the dunite. Amphiboles are occasionally observed at the rim of clinopyroxene (Fig. 4h).

## ANALYTICAL METHODS

All analyses were conducted at the Institute of Geology and Geophysics, Chinese Academy of Sciences, Beijing, China. Detailed procedures, precision, and accuracy of our measurements were presented in the online Supplementary Materials. Briefly, whole rock major element and trace element abundances were obtained using x-ray fluorescence spectroscopy and inductively coupled plasma mass spectrometry (Table S1), respectively. Mineral major element concentrations were determined using a Cameca SX Five electron microprobe (Table S2). Mineral trace elements were obtained by laser ablation inductively coupled plasma mass spectrometry (LA-ICP-MS) (Table 2; Table S3). Neodymium and hafnium isotopic compositions were measured using a Thermo Fisher Neptune plus mass spectrometer (Table 3). In the section ‘Spatial geochemical variations’, the  $\text{Al}_2\text{O}_3$ ,  $\text{Cr}_2\text{O}_3$ , CaO, and  $\text{Na}_2\text{O}$  contents in clinopyroxene and orthopyroxene were obtained by electron microprobe analysis. Other trace element concentrations such as Sc, Dy, Yb, and Y were obtained through LA-ICP-MS (Fig. 8; Appendix 3).

## RESULTS

### Whole rock chemistry

The Xiugugabu pyroxenites are fresh with little alteration (Figs 3 and 4), which is consistent with their low loss on ignition (<0.8 wt.%). Four olivine websterites and one pyroxene-bearing dunite were analyzed for whole rock major elements. The five samples display large variations in  $\text{Al}_2\text{O}_3$  (1.3–3.4 wt.%) and CaO (1.5–9.9 wt.%) (Table S1). Such large variations remain the same within the olivine websterite veins. These samples contain 26.8–43.1 wt.% MgO and 5.3–8.2 wt.%  $\text{FeO}_{\text{Tot}}$ , yielding nearly constant Mg# [ $=100 \times \text{Mg} / (\text{Mg} + \text{Fe}_{\text{Tot}})$ ] of 90–91, reflecting different proportions of orthopyroxene and clinopyroxene. In addition, these samples have remarkably low abundances of  $\text{TiO}_2$ ,  $\text{Na}_2\text{O}$ , and  $\text{K}_2\text{O}$  (all <0.1 wt.%).

In terms of trace elements, the five samples display large variations of REE contents, which correlate with their clinopyroxene abundances. For example, sample

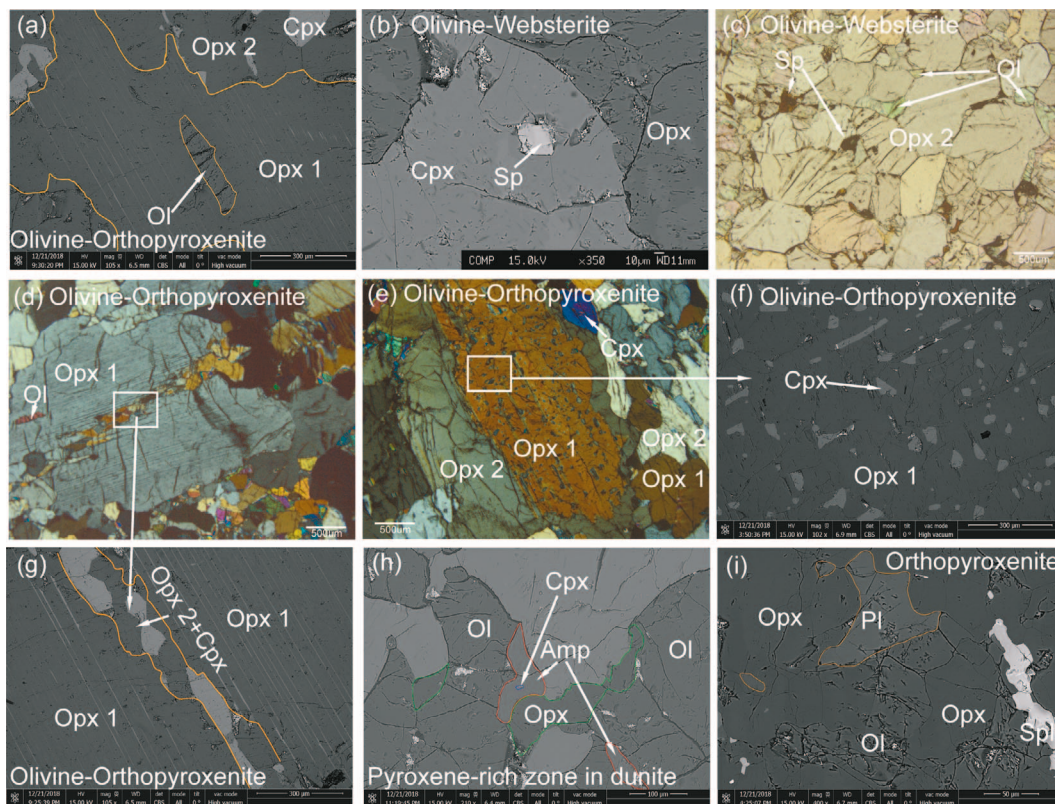


**Fig. 4.** Representative microtextures of the Xiugugabu pyroxene-bearing dunite and pyroxenites. (a) A poikilitic olivine grain was enclosed by orthopyroxene porphyroclast (Opx1), which has extensive clinopyroxene exsolution lamellae. (b) Spinel inclusions in clinopyroxene. (c) Plane-polarized image of recrystallization features (17TP22) with well-developed 120° triple junctions (clinopyroxene-orthopyroxene assemblage). (d–g) Composite vein 17TP19: veinlet of clinopyroxene-orthopyroxene assemblage intrudes the coarse-grained Opx1. (h) Interstitial amphibole occurs at the margin of the clinopyroxene. (i) Interstitial olivine-plagioclase-clinopyroxene-orthopyroxene assemblage in the orthopyroxenite 17TP29. Abbreviations: Amp, amphibole; Pl: plagioclase.

17TP25 has the highest modal clinopyroxene of 58.4% (Table 1) and the highest REE contents. In the chondrite-normalized REE diagram (Fig. 5a), the pyroxene-bearing dunites and pyroxenites show spoon-shaped patterns with flat heavy REE (HREE), depleted middle REE (MREE), elevated light REE (LREE), and exhibit large ranges of REE concentrations ( $Yb_N = 0.7\text{--}2.6$ ) (Fig. 5a). In the primitive mantle normalized spider diagram (Fig. 5b), the Xiugugabu pyroxene-bearing dunite and olivine websterites do not show strong enrichments in LILEs and other fluid-mobile elements (e.g., Rb, Ba, and Sr). Two samples (17TP18-2 and 17TP21) have positive Nb and Ta anomalies and positive Ti anomalies in their bulk rocks. The latter is due to the high proportion of orthopyroxene in the samples (Fig. 5b and d). To assess contributions of clinopyroxene and orthopyroxene to the bulk composition, we reconstructed bulk rock trace element composition using a simple mass balance calculation (equation (5) in Liang et al., 2021). The reconstructed results show a good agreement with their whole rock compositions for the middle and HREE (Fig. 5c). However, LREE, Sr, and HFSE in the reconstructed bulk rock are lower than the measured whole rock values (Fig. 5c and d). This may result from larger analytical uncertainty of the lower concentration LREE in the bulk rock and/or presence of interstitial

minerals (e.g., amphibole and plagioclase) in these samples (Fig. 4h and i).

### Mineral major elements

Average mineral major element compositions of the Xiugugabu pyroxene-bearing dunite, pyroxenites, and their host peridotites are presented in Table S2. Olivines in the pyroxenites and their neighboring peridotites have similar forsterite contents [ $Fo = 100 \times Mg / (Mg + Fe_{Tot})$ ] varying from 89 to 91. Olivine in the pyroxene-bearing dunite (17TP21) has the highest Fo content (92) among the studied samples (Fig. 6a). Overall, olivines in the pyroxenites and pyroxene-bearing dunite commonly have lower Fo and higher NiO contents than those in the peridotites from the YZSZ (Fig. 6a; Appendix 2). Spinel in the studied pyroxenites are heterogeneous in composition, with Cr# [ $= 100 \times Cr / (Cr + Al)$ ] ranging from 22 to 37. Spinel with different morphologies also have different compositions (Appendix 1; Table S2). Specifically, spinels that occur as inclusions within orthopyroxene grains have the lowest Cr# (17–23) compared with spinels that occur either in the symplectites or as chains in the samples (Cr# ranging from 19 to 33) (Table S2; 17TP22 and 17TP25). In addition, spinel from the pyroxene-bearing dunite has the highest Cr# value of 50 (Fig. 6b). Interestingly,  $TiO_2$  content in spinel in the studied

**Table 2:** Average trace element compositions of clinopyroxene and orthopyroxene in the Xiugugabu pyroxenites and pyroxene-bearing dunite

Litho. Cpx	Ol-web. 17TP18-1	Ol-web. 17TP18-2	Web. 17TP19-1	Web. 17TP19-5	Px-b. dun. 17TP21	Ol-web. 17TP22	Ol-web. 17TP25	Ol-web. 17TP30
N	7	18	11	14	8	7	8	5
Sc	50	54	55	51	73	47	48	49
Ti	444	752	652	525	1027	424	490	570
Cr	8339	7662	8788	9251	12 177	4891	7478	6523
Co	27	23	24	26	24	24	24	21
Ni	439	388	410	384	385	365	337	406
Sr	0.07	2.38	0.86	0.67	0.84	0.07	0.13	0.22
Y	3.92	5.93	4.93	3.68	6.79	3.87	4.09	5.81
Zr	b.d.l	b.d.l	0.101	0.093	0.173	0.037	0.049	0.067
Nb	0.019	0.010	0.027	0.029	0.055	0.010	0.006	0.014
Ba	b.d.l	0.091	0.446	0.179	0.291	0.066	0.055	0.190
La	b.d.l	b.d.l	0.005	0.009	0.032	b.d.l	0.002	0.002
Ce	b.d.l	b.d.l	0.014	0.019	0.031	b.d.l	0.005	0.004
Pr	b.d.l	b.d.l	0.008	0.007	0.028	0.001	0.003	0.003
Nd	b.d.l	0.135	0.115	0.124	0.178	0.007	0.078	0.060
Sm	0.035	0.155	0.175	0.156	0.251	0.041	0.159	0.143
Eu	0.022	0.074	0.088	0.077	0.121	0.024	0.077	0.072
Gd	0.203	0.451	0.473	0.352	0.591	0.236	0.332	0.467
Tb	0.056	0.109	0.105	0.081	0.131	0.065	0.077	0.113
Dy	0.589	0.962	0.827	0.659	1.155	0.588	0.716	0.935
Ho	0.153	0.228	0.194	0.147	0.264	0.146	0.169	0.225
Er	0.485	0.704	0.588	0.437	0.784	0.467	0.498	0.706
Tm	0.074	0.100	0.085	0.065	0.116	0.076	0.068	0.100
Yb	0.502	0.707	0.578	0.439	0.793	0.484	0.528	0.686
Lu	0.073	0.097	0.081	0.062	0.113	0.076	0.071	0.097
Hf	b.d.l	b.d.l	0.026	0.019	0.101	0.009	b.d.l	0.022

**Table 2:** Continued

Litho. Opx	Ol-web. 17TP18-1	Ol-web. 17TP18-2	Web. 17TP19-1	Ol-opxnite 17TP19-3	Web. 17TP19-5	Px-b. dun. 17TP21	Ol-web. 17TP22	Ol-web. 17TP25	Ol-opxnite 17TP29	Ol-web. 17TP30
N	10	9	6	10	12	9	6	4	11	8
Sc	25	21	23	22	23	24	22	24	26	22
Ti	177	226	238	199	208	404	149	194	372	191
Cr	4827	4269	4967	5247	4548	4636	4277	4693	3886	5015
Co	60	53	59	68	60	54	61	55	65	60
Ni	789	664	757	841	632	674	707	653	822	815
Sr	0.03	0.03	0.03	0.04	0.03	0.05	0.05	0.02	0.23	0.09
Y	0.49	0.52	0.44	0.45	0.41	0.60	0.43	0.56	0.83	0.61
Zr	0.037	b.d.l	b.d.l	b.d.l	b.d.l	b.d.l	b.d.l	b.d.l	0.042	0.268
Nb	0.014	0.007	0.015	0.016	0.028	0.013	0.012	0.004	0.020	0.007
Ba	b.d.l	b.d.l	b.d.l	0.167	b.d.l	b.d.l	b.d.l	b.d.l	1.102	b.d.l
La	0.001	b.d.l	b.d.l	0.000	b.d.l	b.d.l	0.000	b.d.l	0.005	0.002
Ce	0.001	b.d.l	b.d.l	0.001	b.d.l	b.d.l	b.d.l	b.d.l	0.005	b.d.l
Pr	0.000	b.d.l	0.000	0.001	b.d.l	0.001	0.000	b.d.l	0.001	0.001
Nd	0.001	b.d.l	0.003	0.007	b.d.l	0.014	0.001	b.d.l	0.003	0.004
Sm	0.001	b.d.l	0.003	0.009	b.d.l	0.013	0.001	b.d.l	0.002	0.007
Eu	0.004	b.d.l	0.008	0.004	b.d.l	0.006	b.d.l	b.d.l	0.003	0.006
Gd	0.010	0.039	0.013	0.019	0.020	0.026	0.008	0.021	0.020	0.023
Tb	0.004	0.007	0.004	0.005	0.008	0.006	0.004	0.006	0.007	0.006
Dy	0.048	0.063	0.048	0.055	0.054	0.074	0.043	0.064	0.091	0.069
Ho	0.017	0.018	0.015	0.017	0.014	0.023	0.017	0.022	0.029	0.021
Er	0.078	0.073	0.071	0.067	0.066	0.094	0.073	0.080	0.128	0.089
Tm	0.016	0.014	0.014	0.014	0.011	0.018	0.015	0.018	0.024	0.018
Yb	0.151	0.157	0.135	0.114	0.121	0.152	0.148	0.167	0.227	0.160
Lu	0.027	0.025	0.026	0.020	0.026	0.026	0.026	0.029	0.040	0.030
Hf	0.002	0.009	0.002	0.004	0.004	0.004	0.003	b.d.l	0.009	0.006

Litho. indicates lithology; N, number of measurements; Cpx, clinopyroxene; Opx, orthopyroxene; Ol, olivine; Web., websterite; Px-b. dun., pyroxene-bearing dunite; Opxnite, orthopyroxenite; b.d.l, below detection limit.

Table 3: Nd–Hf isotope ratios of the Xiugugabu pyroxenites and pyroxene-bearing dunite

Sample	Comments	Lithology	Sm	Nd	$^{147}\text{Sm}/^{144}\text{Nd}$	$^{143}\text{Nd}/^{144}\text{Nd}$	$2\sigma$	Lu	Hf	$^{176}\text{Lu}/^{177}\text{Hf}$	$^{176}\text{Hf}/^{177}\text{Hf}$	$2\sigma$	$(^{143}\text{Nd}/^{144}\text{Nd})_i$	$(^{176}\text{Hf}/^{177}\text{Hf})_i$	$\epsilon_{\text{Nd}}(t)$	$\epsilon_{\text{Hf}}(t)$
17TP18 Cpx	Cpx	Olivine-Websterite	0.159	0.101	0.949	0.513507	0.000013	—	—	—	—	—	0.512731	—	5.0	—
17TP18	WR	—	0.007	0.007	0.633	0.512723	0.000041	0.028	0.004	0.889	0.284885	0.000034	0.512205	0.282807	−5.3	4.0
17TP18 (d)	WR	—	0.012	0.012	0.588	0.512612	0.000057	0.029	0.005	0.854	0.284831	0.000062	0.512131	0.282835	−6.8	5.0
17TP19 Cpx	Cpx	Compos-ite	0.191	0.134	0.861	0.513465	0.000014	—	—	—	—	—	0.512761	—	5.5	—
17TP19 Cpx (d)	Cpx	Veins	0.137	0.088	0.941	0.513498	0.000019	0.069	0.050	0.199	0.282785	0.000007	0.512728	0.282321	4.9	−13.2
17TP19 Opx	Opx	—	0.004	0.005	0.505	0.512415	0.000046	0.020	0.006	0.527	0.283733	0.000054	0.512002	0.282503	−9.3	−6.8
17TP19	WR	—	0.022	0.049	0.276	0.512232	0.000019	0.010	0.007	0.213	0.283112	0.000019	0.512006	0.282614	−9.2	−2.8
17TP19 (d)	WR	—	0.022	0.048	0.276	0.512244	0.000022	0.017	0.011	0.214	0.283097	0.000022	0.512018	0.282596	−9.0	−3.5
17TP21	Cpx	Pyroxene-bearing dunite	—	—	—	—	—	0.092	0.042	0.312	0.283478	0.000009	—	0.282750	—	2.0
17TP21	WR	—	0.033	0.028	0.712	0.513225	0.000015	0.017	0.008	0.299	0.283689	0.000025	0.512643	0.282991	3.2	10.5
17TP21 (d)	WR	—	0.052	0.046	0.679	0.513134	0.000028	0.018	0.009	0.282	0.283686	0.000039	0.512578	0.283028	—	11.8
17TP21 (d)	WR	—	0.042	0.037	0.684	0.513183	0.000024	0.022	0.011	0.291	0.283681	0.000022	0.512624	0.283002	2.9	10.9
17TP22 Cpx	Cpx	Olivine-Websterite	—	—	—	—	—	0.075	0.018	0.602	0.283822	0.000014	—	0.282416	—	−9.8
17TP22	WR	—	0.016	0.035	0.280	0.512111	0.000022	0.029	0.009	0.446	0.283726	0.000024	0.511882	0.282684	−11.6	−0.4
17TP22 (d)	WR	—	0.010	0.021	0.288	0.512190	0.000024	0.028	0.008	0.471	0.283744	0.000021	0.511954	0.282643	−10.2	−1.8
17TP22 (d)	WR	—	0.008	0.016	0.287	0.512174	0.000024	0.019	0.006	0.478	0.283779	0.000016	0.511940	0.282662	−10.5	−1.2
17TP25 Cpx	Cpx	Olivine-Websterite	0.172	0.088	1.180	0.514023	0.000011	0.075	0.030	0.351	0.283874	0.000009	0.513058	0.283054	11.3	12.7
17TP25 Opx	Opx	—	0.009	0.036	0.143	0.511556	0.000015	0.025	0.004	0.924	0.285570	0.000040	0.511439	0.283411	−20.3	25.3
17TP25	WR	—	0.063	0.048	0.791	0.513060	0.000014	0.054	0.015	0.510	0.284215	0.000012	0.512413	0.283023	−1.3	11.6
17TP25 (d)	WR	—	0.098	0.074	0.794	0.513019	0.000016	0.055	0.016	0.498	0.284123	0.000017	0.512370	0.282960	−2.1	9.4

WR indicates whole rock; Opx, orthopyroxene; Cpx, clinopyroxene; d, duplicate sample; i, initial isotope ratio. All concentrations are in ppm. Decay constants  $\lambda_{\text{Sm}} = 6.54 \times 10^{-12} \text{ a}^{-1}$  (DePaolo, 1981), and  $\lambda_{\text{Lu}} = 1.867 \times 10^{-11} \text{ a}^{-1}$  (Söderlund *et al.*, 2004) were used to calculate the initial  $^{143}\text{Nd}/^{144}\text{Nd}$  and  $^{176}\text{Hf}/^{177}\text{Hf}$  ratios at 125 Ma (the age of mafic rocks in Xiugugabu ophiolite).  $\epsilon$  values of Nd–Hf isotopes were calculated using the present-day chondritic uniform reservoir values of Sm–Nd system with  $^{147}\text{Sm}/^{144}\text{Nd} = 0.1967$ ,  $^{143}\text{Nd}/^{144}\text{Nd} = 0.512683$ , and for Lu–Hf system,  $^{176}\text{Lu}/^{177}\text{Hf} = 0.0332$ , and  $^{176}\text{Hf}/^{177}\text{Hf} = 0.282772$  (Bouvier *et al.*, 2008).

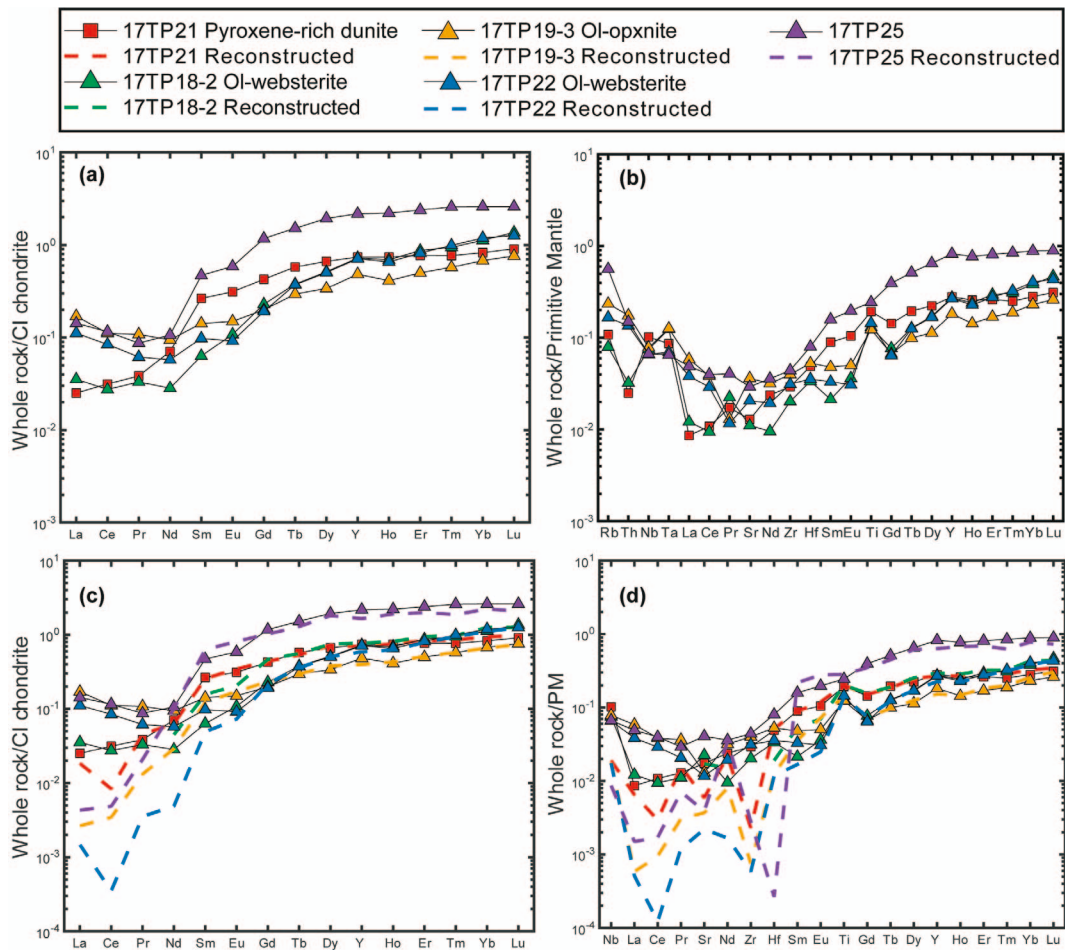


**Fig. 5.** Whole rock compositions in the Xiugugabu dunite and pyroxenites. (a) Chondrite normalized REE patterns (normalization values are from Anders & Grevesse, 1989). (b) Primitive-mantle normalized trace element patterns (normalization values from Palme & O'Neill, 2014). (c, d) Reconstructed trace element compositions (dashed lines).

samples is very low (<0.1 wt.%). In fact, it is lower than those observed in abyssal pyroxenites (Dantas *et al.*, 2007; Warren *et al.*, 2009; Dick *et al.*, 2010; Laukert *et al.*, 2014), pyroxenites from the Oman (Python & Ceuleneer, 2003; Tamura & Arai, 2006; Python *et al.*, 2008), and Josephine ophiolites (Le Roux & Liang, 2019) (Fig. 6b).

In general, orthopyroxene show core-to-rim zonation with decreasing  $\text{Al}_2\text{O}_3$  and  $\text{Cr}_2\text{O}_3$  from the core of coarse-grained orthopyroxene (orthopyroxene 1) to the rim of orthopyroxene 1 and toward the interstitial orthopyroxene neoblasts (orthopyroxene 2) (Fig. 8; Appendix 3; Table S2). Compositional zoning is not observed in clinopyroxene in samples included in this study. Detailed variations across pyroxenites and their host peridotite are discussed in the section 'Spatial Geochemical Variations'. Pyroxenes in the studied samples contain relatively low  $\text{Al}_2\text{O}_3$  (1.9–3.6 wt.% for orthopyroxene and 2.5–4.3 wt.% for clinopyroxene; Fig. 6c and e). The pyroxene-bearing dunite has the highest Mg# in orthopyroxene (92) and clinopyroxene (94), and the highest  $\text{Na}_2\text{O}$  (0.53 wt.%) and  $\text{TiO}_2$  (0.17 wt.%) contents in clinopyroxene among the studied samples (Fig. 6f). Compared with orthopyroxene from the residual

peridotites, orthopyroxene in the pyroxenites have lower Mg# values (89 to 92) but similar  $\text{Al}_2\text{O}_3$  and  $\text{TiO}_2$  contents (Fig. 6c and d; Appendix 2). Clinopyroxenes in the Xiugugabu pyroxenites ( $\text{Wo}_{46-49}\text{En}_{46-50}\text{Fs}_{3-4}$ ) are Cr-diopside in composition ( $\text{Cr}_2\text{O}_3$ : 0.71–1.38 wt.%), and they have high Mg# (92–93), low  $\text{TiO}_2$  (0.07–0.18 wt.%), and  $\text{Na}_2\text{O}$  (0.06–0.27 wt.%) contents.

Amphibole identified in two samples (17TP20 and 17TP25; Fig. 4h) occurs at the rims of clinopyroxene and contains 10.6–13.1 wt.%  $\text{Al}_2\text{O}_3$  and 1.0–3.1 wt.%  $\text{Na}_2\text{O}$  and has high Mg# (91–93; Table S2). According to the classification of Leake *et al.* (1997), they are pargasite and magnesio-hornblende. In highly serpentinized abyssal peridotites, amphibole formed during seawater alteration is typically tremolitic in composition and associated with talc (e.g., Dick *et al.*, 2010). The amphiboles observed in the two samples (17TP20 and 17TP25) are different in compositions from the amphiboles produced by seawater alteration. Finally, plagioclases are found in the orthopyroxenite 17TP29 (Fig. 4i). They are nearly pure anorthite with An content [ $\text{An} = 100 \times \text{Ca} / (\text{Ca} + \text{Na} + \text{K})$ ] of 97–98 (Table S2).

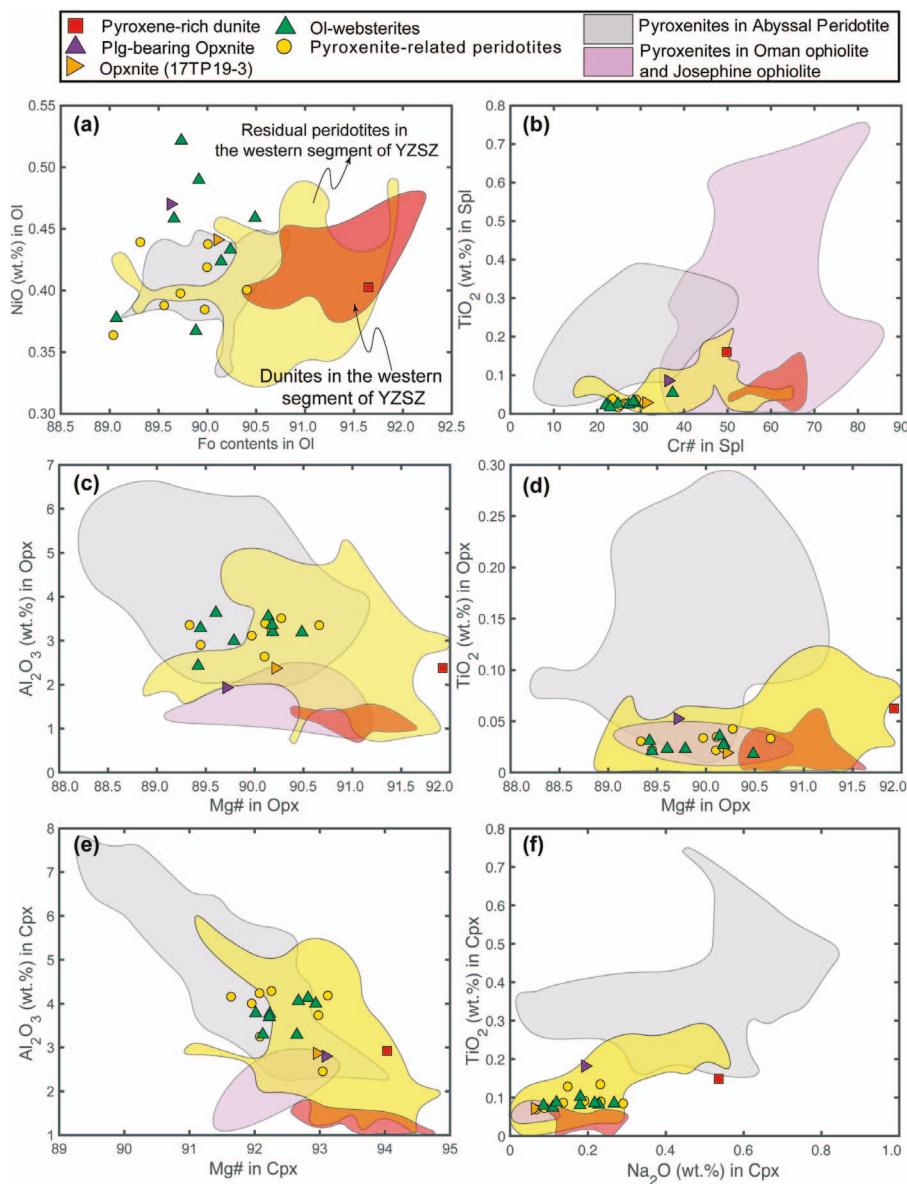


**Fig. 6.** Selected major element compositions of olivine (a), spinel (b), orthopyroxene (c and d), and clinopyroxene (e and f) in the Xiugugabu pyroxene-bearing dunite and pyroxenites. Abyssal pyroxenites are from (Dantas *et al.*, 2007; Dick *et al.*, 2010; Laukert *et al.*, 2014; Warren *et al.*, 2009). The Oman pyroxenites (Python & Ceuleneer, 2003; Python *et al.*, 2008; Tamura & Arai, 2006), Josephine pyroxenites (Le Roux & Liang, 2019), and Marum orthopyroxenites (Kaczmarek *et al.*, 2015) are shown for comparison. Lherzoliths and harzburgites in the western segment of YZSZ are from (Gong *et al.*, 2016; Guo *et al.*, 2015; Lian *et al.*, 2016; Liu *et al.*, 2014; Su *et al.*, 2015). Dunites in the western segment are from (Guo *et al.*, 2015).

### Mineral trace elements

Trace element concentrations of clinopyroxene and orthopyroxene in the Xiugugabu pyroxene-bearing dunite and pyroxenites are reported in Table S3. Sample averages are provided in Table 2. Neither amphibole nor plagioclase was measured for trace elements due to their small grain sizes. To better capture the chemical variations along the transect (Fig. 8), we focused our analytical effort on different mineral grains that include the rim of orthopyroxene 1, cores of orthopyroxene 2, and clinopyroxene within each pyroxenite vein. Most orthopyroxene show an increase in incompatible element concentration from core to rim (Table S3). In contrast, the cores of porphyroclastic orthopyroxene in the plagioclase-bearing orthopyroxenite (17TP29) have

higher contents of incompatible trace elements than the rims (Appendix 3; Table S3).

Clinopyroxenes in the Xiugugabu pyroxenites have a characteristic spoon-shaped REE pattern with flat MREE to HREE, Ce to Sm depletion, and a mild La enrichment (Fig. 7a). In the primitive mantle normalized spider diagram, they show a moderate enrichment in Ba and Nb relative to La but varying negative anomalies in Zr and Hf relative to Nd and Sm (Fig. 7c). Orthopyroxenes from all the Xiugugabu pyroxenites typically display LREE-depleted patterns (Fig. 7b). In the primitive mantle normalized diagram, they show a strong positive Ti anomaly and a mild positive Hf anomaly (Fig. 7d). Trace element patterns of clinopyroxene and orthopyroxene are very similar to those of residual peridotites from the YZSZ

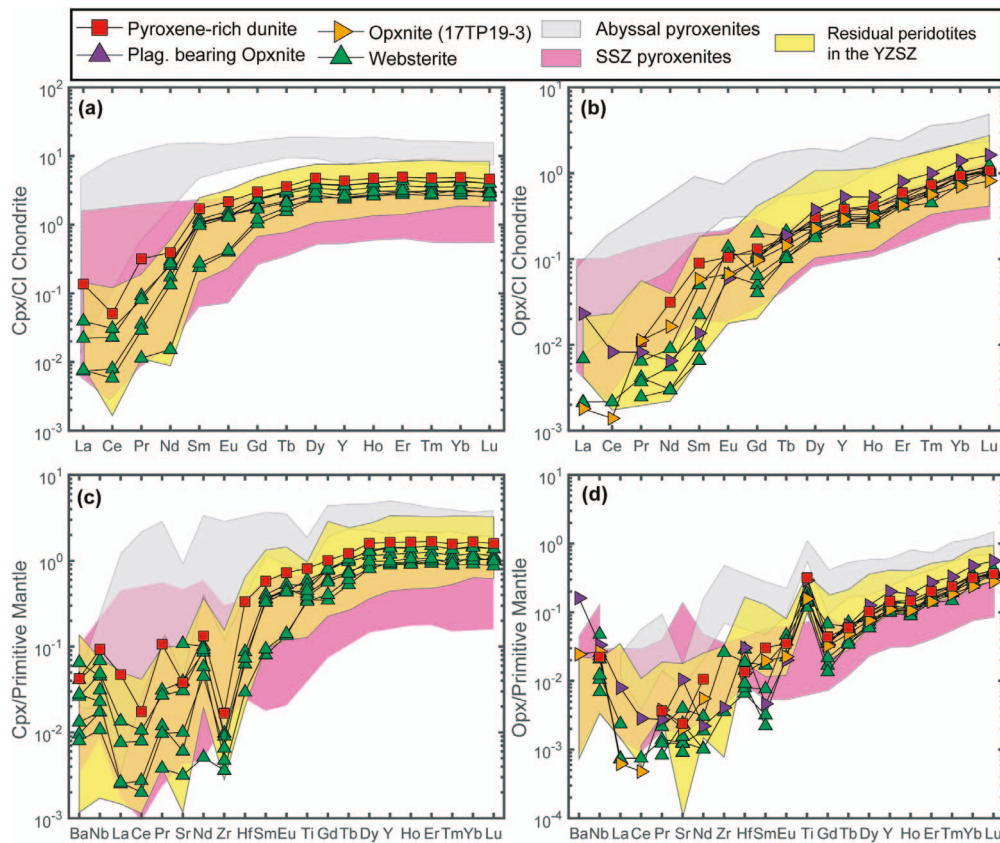


**Fig. 7.** Chondrite (Anders & Grevesse, 1989) normalized REE and primitive mantle (Palme & O'Neill, 2014) normalized trace element patterns of clinopyroxene and orthopyroxene. Also shown as color-coded fields are compositions of clinopyroxene in Oman orthopyroxenites (Tamura & Arai, 2006), Josephine pyroxenites (Le Roux & Liang, 2019), and Marum pyroxenites (Kaczmarek et al., 2015) and compositions of orthopyroxene in Josephine pyroxenites (Le Roux & Liang, 2019) and Marum orthopyroxenites (Kaczmarek et al., 2015). The data source of abyssal pyroxenites is the same as those in Fig. 6. The compositional regions of clinopyroxene and orthopyroxene in the residual peridotites in the Purang ophiolite (Gong et al., 2020) and the Zedong ophiolite (Xiong et al., 2017b).

(Fig. 7a–d). Pyroxenes in the Xiugugabu pyroxenites have higher REE contents than those pyroxenites from the Oman ophiolite (Tamura & Arai, 2006), the Josephine ophiolite (Le Roux & Liang, 2019) and the Marum ophiolites (Kaczmarek et al., 2015). As shown in Fig. 7, pyroxenites from the aforementioned ophiolites are generally more depleted in incompatible trace elements than abyssal pyroxenites (Dantas et al., 2007; Warren et al., 2009; Laukert et al., 2014).

### Spatial geochemical variations

Spatial compositional variations are observed on the grain scale and thin-section scale for the composite dunite-orthopyroxenite-websterite vein 17TP19 (Fig. 8). The  $\text{Al}_2\text{O}_3$  concentrations in orthopyroxene and clinopyroxene increase from dunite to websterite (Fig. 8a and e; Table S2). In the websterite-harzburgite section (17TP19-5), the coarse-grained orthopyroxene has higher  $\text{Al}_2\text{O}_3$  content (3.50–3.82 wt.%) than the fine-grained orthopyroxene (2.59–3.59 wt.%  $\text{Al}_2\text{O}_3$ ). Orthopyroxene in the dunite-orthopyroxenite section (17TP19-3) has the lowest  $\text{Al}_2\text{O}_3$  concentration (1.70–2.78 wt.%). The  $\text{Al}_2\text{O}_3$  concentration profiles are approximately symmetric across the lithological sequence (Fig. 8a and e). The systematic variation is also observed for  $\text{Cr}_2\text{O}_3$  in

orthopyroxene and clinopyroxene (Fig. 8b and f). It is worth noting that clinopyroxene in the orthopyroxenite and dunite has a steep drop in  $\text{Na}_2\text{O}$  concentration relative to clinopyroxene in the surrounding websterite (Fig. 8g). Additionally, we analyzed one coarse grained orthopyroxene and its clinopyroxene exsolution lamellae (clinopyroxene 2 in Fig. 4f). The host orthopyroxene has 2.97–3.30 wt.%  $\text{Al}_2\text{O}_3$ , whereas the exsolved clinopyroxene has 3.65–3.72 wt.%  $\text{Al}_2\text{O}_3$  that is slightly lower than clinopyroxene neoblasts (3.86–4.04 wt.%) near the orthopyroxene.

Thin-section scale spatial major element variations of other samples are presented in Appendix 3. They share some similarities with the composite dunite-orthopyroxenite-websterite vein 17TP19: (1) most samples show gradual chemical variations from dunite through pyroxenites to host harzburgite, whereas orthopyroxene in the plagioclase-bearing orthopyroxenite has abrupt variations of  $\text{Al}_2\text{O}_3$ , changing from 1.65–2.25 wt.% in veins to 3.40–3.63 wt.% in the host harzburgite; (2) both clinopyroxene and orthopyroxene show decreasing trend of  $\text{Al}_2\text{O}_3$  contents in the order of dunite, pyroxenite, and host harzburgite.

Concentration profiles of trace elements are incomplete across the lithological sequence. Our limited

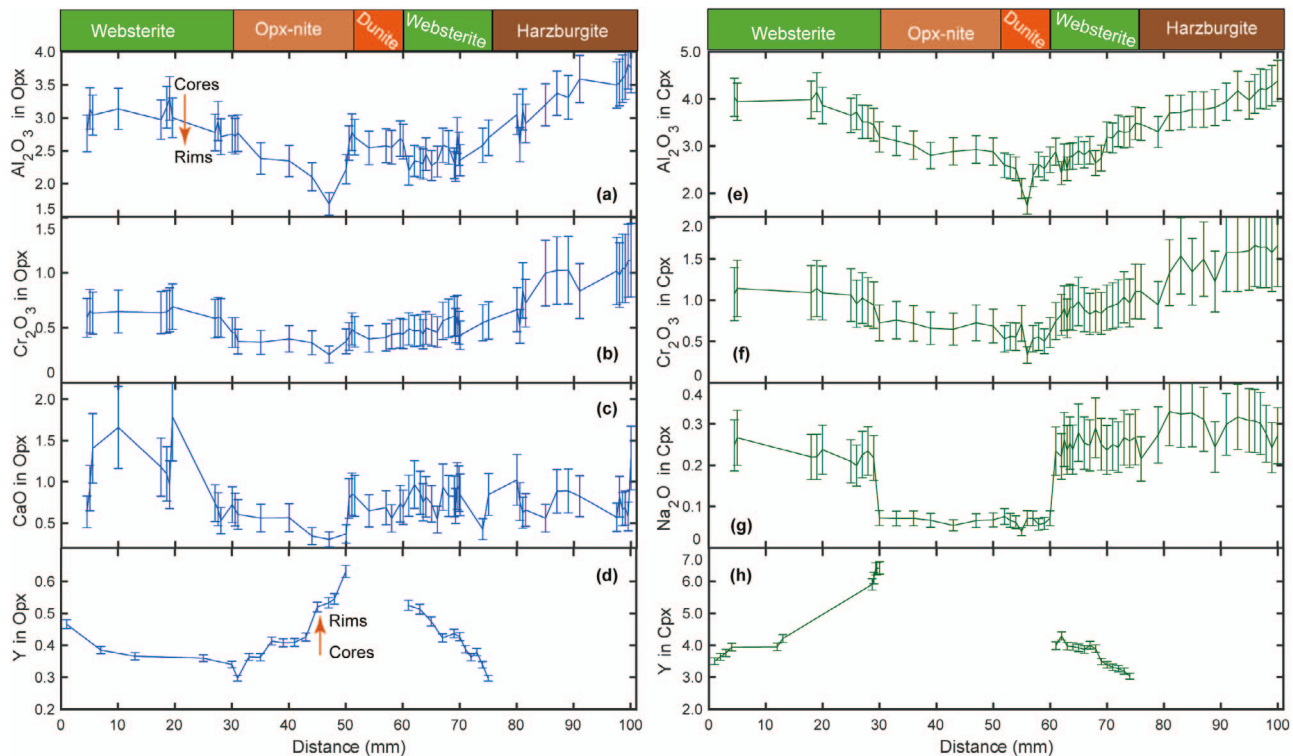


**Fig. 8.** Spatial variations in selected major and trace elements in orthopyroxenes and clinopyroxenes from the composite dunite-orthopyroxenite-websterite vein (17TP19). The error bars are the standard deviation ( $1\sigma$ ) about the mean of all analyses of orthopyroxene and clinopyroxene for a particular lithology. The thick arrows in (a) and (c) indicate the core to rim composition variations in the porphyroclastic orthopyroxenes.

data suggest that concentrations of incompatible trace elements in orthopyroxene and clinopyroxene are inversely correlated with concentrations of  $\text{Al}_2\text{O}_3$  in the pyroxenes. This trend is also true for grain scale core-to-rim variations. Figure 8d and h shows examples of Y concentration profiles measured by LA-ICP-MS. Concentration profiles of other incompatible elements are presented in Appendix 3.

### Temperature estimates for the Xiugugabu pyroxenites and pyroxene-bearing dunite

Primary P–T conditions of the Xiugugabu mantle section were overprinted by late-stage melt percolation events and subsequent cooling. Although there are no suitable geobarometers for garnet-free ultramafic rocks, the pressure of these pyroxenites can be evaluated indirectly. The occurrence of anorthitic plagioclase ( $\text{An} = 97\text{--}98$ ) in the plagioclase-bearing orthopyroxenite 17TP29 suggests that the pyroxenite can reach shallow levels of the upper mantle ( $\sim 0.7$  GPa; Borghini *et al.*, 2010). Spinel is the dominant aluminous phase in the Xiugugabu pyroxenites, which suggests that they represent magmatic products derived from relatively high pressure. For a pyroxenitic bulk composition, the breakdown of spinel into plagioclase (Fig. 4i; spinel + orthopyroxene + clinopyroxene  $\rightarrow$  plagioclase + olivine) occurs at 0.6–0.7 GPa (Gasparik, 1984). In addition, high-Al amphiboles (pargasite and magnesio-hornblende) that coexist with olivine, pyroxenes, and spinel have a narrow stability field of

850°C–1050°C and 0.8–1.7 GPa (Grove *et al.*, 2006). Overall, a pressure of 0.7–1.5 GPa seems a reasonable estimate for the formation of the Xiugugabu pyroxenitic samples.

Assuming a pressure of 1.0 GPa for the pyroxene-bearing dunite and pyroxenites, equilibrium or closure temperatures for the studied lithologies were obtained using pyroxene thermometers (Brey & Köhler, 1990; Liang *et al.*, 2013). The results are presented in Table 1 and Appendix 4. The temperature estimates of the pyroxenites are calculated using methods of Mg–Fe exchange between clinopyroxene and orthopyroxene and Ca solubility in orthopyroxene (Brey & Köhler, 1990). REE closure temperatures were obtained by linear fitting of the apparent partition coefficients of REE between coexisting clinopyroxene and orthopyroxene. Some LREE (e.g., La, Ce, Pr, Nd) are excluded as they showed significant deviations from the trend defined by other REE in the inversion diagram (Appendix 5). In general, the REE-based temperatures are higher than major-element based temperatures ( $T_{\text{REE}} > T_{\text{Ca}} > T_{\text{BKN}}$  in Appendix 4), which is consistent with closure temperatures for REE, Ca, and Fe–Mg diffusion in pyroxenes (Zhang *et al.*, 2009; Cherniak & Dimanov, 2010; Liang *et al.*, 2013; Dygert *et al.*, 2017). The closure temperatures of the pyroxene-bearing dunite and pyroxenites generally overlap with the fields of MOR-affinity peridotites and SSZ-affinity peridotites. Two olivine websterite samples (17TP18-1 and 17TP30 in Appendix 4a) have higher  $T_{\text{REE}}$  at a given  $T_{\text{BKN}}$ , indicating

a possible multistage thermal-magmatic history (Le Roux & Liang, 2019).

### Nd–Hf isotopes

For the five samples that we reported whole rock major and trace element compositions, we also measured the Nd–Hf isotope compositions of the whole rock, clinopyroxene, and orthopyroxene. The results are presented in Table 3 and Fig. 9. Large variations in  $^{147}\text{Sm}/^{144}\text{Nd}$  (0.143–1.180),  $^{143}\text{Nd}/^{144}\text{Nd}$  (0.511156–0.514023),  $^{176}\text{Lu}/^{177}\text{Hf}$  (0.199–0.924), and  $^{176}\text{Hf}/^{177}\text{Hf}$  (0.282785–0.285570) are observed for the studied samples. The initial  $^{143}\text{Nd}/^{144}\text{Nd}$ ,  $^{176}\text{Lu}/^{177}\text{Hf}$ ,  $\epsilon_{\text{Nd}}$ , and  $\epsilon_{\text{Hf}}$  values calculated at the age of diabase/gabbroic dike intrusions in the Xiugugabu peridotites (125 Ma), and those values varied from 0.511439 to 0.513058 for  $^{143}\text{Nd}/^{144}\text{Nd}$  ( $\epsilon_{\text{Nd}}(t) = -20.3$  to  $+11.5$ ) and 0.282321–0.283411 for  $^{176}\text{Lu}/^{177}\text{Hf}$  ( $\epsilon_{\text{Hf}}(t) = -13.2$  to  $+25.3$ ) (Fig. 9a). In the initial  $^{147}\text{Sm}/^{144}\text{Nd}$ – $^{143}\text{Nd}/^{144}\text{Nd}$  diagram, the Xiugugabu pyroxenites define a broad positive correlation with more depleted samples overlapping with YZSZ peridotites (Fig. 9b; Appendix 8a). In the  $^{176}\text{Lu}/^{177}\text{Hf}$ – $^{176}\text{Hf}/^{177}\text{Hf}$  diagram, they show a roughly positive covariation (Fig. 9c; Appendix 8b). Importantly, the Xiugugabu pyroxenites show no overlap in initial Nd and Hf isotope ratios with the mafic rocks from YZSZ (Fig. 9b and c), suggesting the lack of genetic relationship between the two.

## DISCUSSION

### Origin of the Xiugugabu pyroxenites and pyroxene-bearing dunite

The studied pyroxenites are mostly tabular or elongated and have sharp boundaries with their associated harzburgites or dunites (Figs 2a, b, and d and 3). In most cases, pyroxenite veins are lithologically symmetric around dunite, forming a dunite–orthopyroxenite–websterite or dunite–websterite sequence (Appendix 1). Both olivine and spinel in the pyroxenites are of residual origin, as they exhibit similar microstructural and compositional features relative to those in the host peridotites (Figs 3b and 6a and b; Figure S1 in Appendix 2). A few orthopyroxene porphyroclasts, occurring at the boundary between the orthopyroxenite vein and the host peridotite and containing abundant clinopyroxene exsolution lamellae (orthopyroxene 1 in Fig. 4d–g), are also residual phases, as their  $\text{Al}_2\text{O}_3$  and  $\text{CaO}$  concentrations are higher than the orthopyroxene neoblasts (e.g., 17TP19 in Table S2). Most porphyroclastic orthopyroxenes in the pyroxenite veins show no or thin clinopyroxene exsolution lamellae (orthopyroxene 2 in Fig. 4d, e, and g) and their  $\text{Al}_2\text{O}_3$  and  $\text{CaO}$  contents are comparable with the fine-grained orthopyroxene in the matrix and lower than those in the host harzburgite (e.g., olivine websterite 17TP18-1 in Appendix 3). These porphyroclastic orthopyroxenes are chemically zoned in major and incompatible trace element concentrations (e.g., plagioclase-bearing orthopyroxenite 17TP29 in Table S3) and might have

crystallized from a silica-rich,  $\text{Al}_2\text{O}_3$ - and incompatible element-depleted melt. Fine-grained orthopyroxene and clinopyroxene in the matrix (i.e., orthopyroxene 2 and clinopyroxene 2) within the Xiugugabu pyroxenites were crystallized from a later melt that infiltrated the host peridotites. The crystallization sequence of orthopyroxene followed by orthopyroxene + clinopyroxene is supported by the observations that newly formed coarse-grained orthopyroxene is surrounded by fine-grained clinopyroxene and orthopyroxene neoblasts (Figs 3 and 4d), and the orthopyroxenes from orthopyroxenites have higher Mg# and lower contents of  $\text{Al}_2\text{O}_3$  than those in orthopyroxenes from websterites (Figs 6c and 10c). The two generations of orthopyroxenes suggest complex melt-peridotite interaction processes involving dissolution of the residual orthopyroxene in the surrounding harzburgite and precipitation of neoblasts of orthopyroxene and clinopyroxene in the pyroxenite veins (e.g., Liang, 2003).

Given the high Mg# in the pyroxenitic clinopyroxene (92–93) and orthopyroxene (89–91) and the presence of amphibole, we hypothesize that the infiltrating hydrous melts were originally in equilibrium with a mantle peridotite that had an Mg# similar to that of the Xiugugabu peridotites (Fig. 6). To test this hypothesis, we carried out batch and fractional crystallization simulations using the thermodynamic program alphaMELTS2 for five choices of melt compositions (Ghiorso & Sack, 1995; Asimow & Ghiorso, 1998; Ghiorso et al., 2002; Smith & Asimow, 2005). We consider an anhydrous primitive MORB, a hydrous basalt (ID-16), a hydrous basaltic andesites (JR-28), a low-Ca boninite (BON IB), and a high-Ca boninite (CY106) (Table 4). The composition of the primitive MORB (Mg# = 75) is the aggregated melt produced by 10% near fractional melting of DMM using alphaMELTS2. The four hydrous melts have high Mg# (69–80) and are considered primitive based on previous studies (Falloon & Danyushevsky, 2000; Weaver et al., 2011; Grove et al., 2012; Woelki et al., 2018). We started crystallization from the liquidus to 200°C below the liquidus at 1°C/step and at pressures of 1.0 GPa for the anhydrous melt and 1.5 GPa for the hydrous melts. The higher pressure (1.5 GPa) used here for hydrous melts is intended to make our crystallization sequences derived from thermodynamic calculations match those derived from experimental studies. For instance, in the phase equilibria experiment of basaltic andesite (JR-28) with 3 wt.% water, olivine is on the liquidus at 1.0 GPa (Weaver et al., 2011). However, in our modeling at 1.0 GPa, the crystallization sequence was orthopyroxene followed by clinopyroxene (Fig. 3 vs Fig. 4 in Appendix 6). Our goal here is to evaluate whether the inferred crystallization sequences and trends of major element variations in clinopyroxene and orthopyroxene in the studied pyroxenites can be explained by the crystallization of basaltic melts. Appendix 6 presents details of our simulation results for each melt composition. Below,

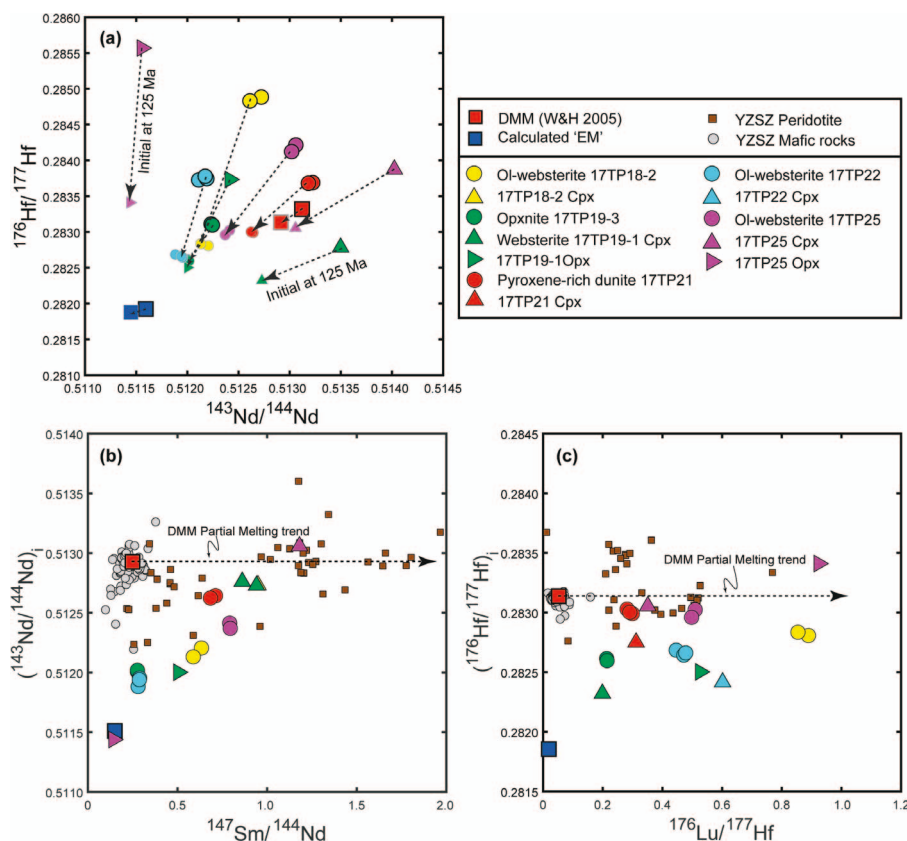


**Fig. 9.** Correlations of isotope ratios in the system Sm–Nd–Lu–Hf. (a)  $^{143}\text{Nd}/^{144}\text{Nd}$  versus  $^{176}\text{Hf}/^{177}\text{Hf}$  for the whole rock, clinopyroxene and orthopyroxene. Arrows connect present-day (large solid symbols) and initial values (small pale symbols). (b) Present date  $^{147}\text{Sm}/^{144}\text{Nd}$  versus initial  $^{143}\text{Nd}/^{144}\text{Nd}$ . (c) Present-day  $^{176}\text{Lu}/^{177}\text{Hf}$  versus initial  $^{176}\text{Hf}/^{177}\text{Hf}$ . The errorbars for  $^{143}\text{Nd}/^{144}\text{Nd}$  and  $^{176}\text{Hf}/^{177}\text{Hf}$  are smaller than size of symbols. The initial  $^{143}\text{Nd}/^{144}\text{Nd}$  and  $^{176}\text{Hf}/^{177}\text{Hf}$  ratios are calculated at 125 Ma. Data source of Nd–Hf isotope compositions of the YZSZ mafic rocks (Li, 2013, Liu et al., 2018b, Mahoney et al., 1998, Miller et al., 2003, Niu et al., 2006, Xiong et al., 2016, Xu & Castillo, 2004, Zhang, 2017, Zhang et al., 2016a, 2016b, Zhang et al., 2005) and the YZSZ residual peridotites (Cheng et al., 2011, Liu et al., 2017, Miller et al., 2003, Xiong et al., 2016, Xiong et al., 2017b, Zhang, 2017, Zhang et al., 2020b, Zhang, 2014) are plotted for comparison. The depleted MORB mantle is from (Workman & Hart, 2005). The ‘enriched mantle’ composition that is calculated by mixing 1% sediments (GLOSS-II) with 99% residual lherzolite (09-ZH-51). Dashed horizontal lines in (b) and (c) represent trends of partial melting of the depleted MORB mantle.

we summarize key conclusions derived from these simulations.

Olivine is on the liquidus of the anhydrous primitive MORB melt at 1.0 GPa. Clinopyroxene starts to crystallize with olivine  $\sim 40^\circ\text{C}$  below the liquidus. Orthopyroxene crystallizes near the end of the simulation at  $\sim 1150^\circ\text{C}$ . The mineral modal abundances at the end of simulations are 87.6% clinopyroxene, 0.9% orthopyroxene, and 11.5% spinel. This is in good agreement with phase equilibria studies of MORB crystallization (e.g., Green & Ringwood, 1967; Elthon & Scarfe, 1984; Villiger et al., 2007). Concentrations of  $\text{Al}_2\text{O}_3$  in clinopyroxene crystallized from the MORB melt range from 6.0 to 12.8 wt.%, which are considerably higher than the  $\text{Al}_2\text{O}_3$  content of clinopyroxene in the Xiugugabu pyroxenites (Fig. 1 in Appendix 6). Hence, anhydrous MORB is an unlikely candidate for the parental melt of the Xiugugabu pyroxenites.

The crystallization sequence of hydrous arc magmas depends on the melt composition and water content. Orthopyroxene is on the liquidus of the boninite melt at 1.5 GPa (BON IB with 3 wt.%  $\text{H}_2\text{O}$  at 1.5 GPa; Fig. 5 in Appendix 6). Clinopyroxene is not a liquidus phase until 48% crystallization. High  $\text{Al}_2\text{O}_3$  and  $\text{TiO}_2$  contents

in the clinopyroxene crystals are not consistent with the Xiugugabu pyroxenites (Fig. 5 in Appendix 6). At 1.5 GPa, the crystallization sequence of basalt ID-16 (with 3 wt.%  $\text{H}_2\text{O}$ ) is orthopyroxene (0%–10% crystallization), followed by clinopyroxene (12%–44% crystallization) (Fig. 2 in Appendix 6). A similar crystallization sequence is observed for both basaltic andesite JR-28 (3 wt.%  $\text{H}_2\text{O}$ ) (Fig. 4 in Appendix 6) and the high-Ca boninite (3 wt.%  $\text{H}_2\text{O}$ ) (Fig. 8 in Appendix 6). Our modeling results are consistent with previous experimental studies on crystallization of hydrous primitive arc magmas (Müntener et al., 2001; Weaver et al., 2011; Wang et al., 2016b), lending support to the inference that the Xiugugabu pyroxenites were crystallized from hydrous melts.

Experiments on the liquid lines of descent of primitive mantle-derived melts show that increasing water content in the melt and decreasing pressure would suppress orthopyroxene stability and extend the temperature interval of clinopyroxene crystallization (e.g., Elthon & Scarfe, 1984; Müntener et al., 2001; Weaver et al., 2011). With increasing extent of crystallization, the Mg#s of clinopyroxene and orthopyroxene decrease, and

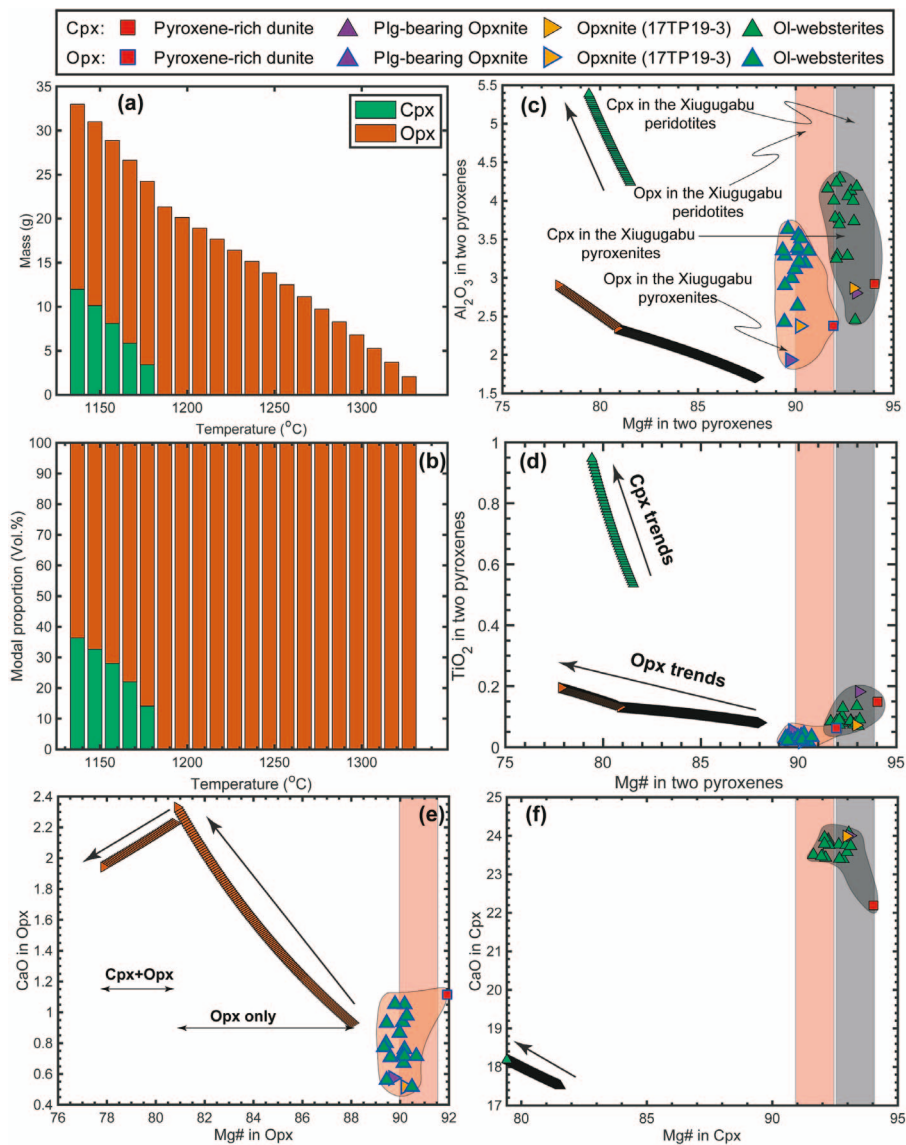


**Fig. 10.** Crystallization sequences and variations of major element compositions of clinopyroxene and orthopyroxene during the AlphaMELTS2 model of batch crystallization of modified hydrous basaltic andesite 'JR-28'. (a) Temperature ( $^{\circ}\text{C}$ ) vs mass (g) of crystallized phases; (b) temperature ( $^{\circ}\text{C}$ ) vs modal proportion (vol.%); (c) Mg# (mol%) vs  $\text{Al}_2\text{O}_3$  contents in orthopyroxene and clinopyroxene; (d) Mg# (mol%) vs  $\text{TiO}_2$  contents in orthopyroxene and clinopyroxene; (e) Mg# (mol%) vs CaO contents in orthopyroxene; (f) Mg# (mol%) vs CaO contents in clinopyroxene. The Mg# variations in orthopyroxene and clinopyroxene in the Xiugugabu peridotites (Bezard *et al.*, 2011) are shown for comparison. See text for discussion.

$\text{Al}_2\text{O}_3$  and  $\text{TiO}_2$  within clinopyroxene and orthopyroxene increase (Appendix 6). Experimental study of basaltic andesite JR28 show that it was formed from partial melting of a depleted harzburgite (Weaver *et al.*, 2011). The  $\text{Al}_2\text{O}_3$  and CaO contents in crystallized clinopyroxene and orthopyroxene are higher than those in the Xiugugabu pyroxenitic clinopyroxene and orthopyroxene (Appendix 6). Hence, the parental melt for the Xiugugabu pyroxenites should have lower contents of  $\text{Al}_2\text{O}_3$  and CaO than JR28. This can be further tested by decreasing  $\text{Al}_2\text{O}_3$  and CaO in the starting melt of JR28 from 16.2 to 10 wt.% for  $\text{Al}_2\text{O}_3$  and from 8.4 to 7.0 wt.% for CaO, while keeping proportions of other major elements the same. The orthopyroxene crystallized from the new melt cover the variations of  $\text{Al}_2\text{O}_3$  and  $\text{TiO}_2$  contents of orthopyroxene in the Xiugugabu pyroxenites (Fig. 10c and d). The increase

of  $\text{Al}_2\text{O}_3$  and CaO in orthopyroxene in the Xiugugabu pyroxenite veins from the orthopyroxenites toward the websterites (Fig. 10c and e) may result from crystallization of the orthopyroxene during the inflow of melt into the system. However, the clinopyroxenes crystallized from the hydrous magma are of much lower Mg# than the clinopyroxenes in the Xiugugabu pyroxenite veins (Figs. 10e and f). Hence, clinopyroxenes in the Xiugugabu pyroxenite veins cannot be crystallized from the same batches of melt as orthopyroxenes. Multiple episodes of melt infiltration therefore are likely involved and the clinopyroxene in the Xiugugabu pyroxenites may result from crystallization of a later batch of melt.

The concentration profiles across the composite dunite–orthopyroxenite–websterite–harzburgite vein system of sample 17TP19 lend support to this hypothesis

**Table 4:** Primitive melt compositions used to derive their crystallization sequences and variations of mineral major elements

Description	Calculated primitive MORB	ID16 <sup>1</sup>	JR-28 <sup>2</sup>	BON IB <sup>3</sup>	CY106 <sup>4</sup>
Pressure (GPa)	1.0	1.5	1.5	1.5	1.5
H <sub>2</sub> O (wt.%)	0.0	3.0	3.0	2.5	3.0
SiO <sub>2</sub>	46.0	48.9	53.2	51.9	54.2
TiO <sub>2</sub>	0.7	0.7	0.8	0.7	0.3
Al <sub>2</sub> O <sub>3</sub>	17.5	16.0	16.2	8.7	14.0
FeO(T)	8.7	8.8	7.6	8.9	7.7
MnO	0.0	0.2	0.1	0.1	0.1
MgO	13.9	11.4	9.4	20.7	9.4
CaO	10.3	10.9	8.4	7.1	12.6
Na <sub>2</sub> O	2.9	2.2	3.4	1.7	0.8
K <sub>2</sub> O	0.0	0.5	0.8	0.2	0.1
P <sub>2</sub> O <sub>5</sub>	100.0	0.1	0.2	0.0	0.0
Molar Mg#	75	70	70	80	69

P, pressure in GPa; H<sub>2</sub>O contents in weight percent (wt.%). Mg# = 100\*(Mg/Mg + FeO<sub>Tot</sub>). Subscript notes are data source from 1 and 2. Weaver et al., 2011; 3. Falloon & Danyushevsky, 2000; 4. Woelki et al., 2018. Calculated primitive MORB were derived from aggregated melt composition from 0% to 10% decompression melting of DMM (Table S4).

(Fig. 8). Two endmembers are needed to interpret the concentration profiles: (1) a residual harzburgite or lherzolite and (2) a hydrous melt that is depleted in Al<sub>2</sub>O<sub>3</sub>, TiO<sub>2</sub>, and Na<sub>2</sub>O. Variations of Al<sub>2</sub>O<sub>3</sub> in clinopyroxene and orthopyroxene across the vein system and the steep drop in Na<sub>2</sub>O content in clinopyroxene in the dunite and orthopyroxenite (Fig. 8) may be attributed to infiltration of a depleted melt from the dunite channel into the residual peridotite or a mixing process involving an Al<sub>2</sub>O<sub>3</sub>- and Na<sub>2</sub>O-depleted melt in the dunite and a second melt that is less depleted in Al<sub>2</sub>O<sub>3</sub> produced by hydrous melting of the relatively fertile residual peridotite from below.

In summary, the early crystallization of orthopyroxene, the low contents of Al<sub>2</sub>O<sub>3</sub>, CaO, and TiO<sub>2</sub> in the orthopyroxene, and the presence of interstitial amphibole and nearly pure anorthite (Fig. 4h) in the Xiugugabu pyroxenites suggest that the Xiugugabu pyroxenites were crystallized from a hydrous melt that is depleted in Al<sub>2</sub>O<sub>3</sub>, TiO<sub>2</sub>, and Na<sub>2</sub>O. Such a melt is unlikely to be formed beneath an MOR spreading center. The hydrous melt could be produced by hydrous melting of previously depleted peridotites (Kelemen et al., 1997; Python & Ceuleneer, 2003; Marchesi et al., 2009; Bénard et al., 2018; Le Roux & Liang, 2019). Chemical variations in clinopyroxene across the vein system can be accounted for by multiple episodes of melt flow and melt-rock reaction. The higher Mg# of orthopyroxene and clinopyroxene in the pyroxenite and dunite veins are likely buffered by the host peridotite via dissolution and reprecipitation (Fig. 10).

### Enriched and depleted mantle components as deduced from initial Nd–Hf isotopes

The initial Nd–Hf isotopic compositions of the Xiugugabu pyroxenite veins reported here extend to more unradiogenic Nd–Hf isotopic compositions than those of MORB and OIB (Fig. 11a). This is in stark contrast to basalts and peridotites from the YZSZ that have initial Nd–Hf isotope compositions similar to present-day MORB (Fig. 11a). The large Nd–Hf isotopic variations

of the Xiugugabu pyroxenite veins can be explained by mixing of melts derived from a depleted endmember and an enriched endmember. The depleted endmember has initial Nd and Hf isotope ratios similar to those of DMM (Fig. 11a). Here, we use the average age-corrected Nd–Hf isotopic compositions of the YZSZ peridotites as the Nd–Hf isotopic compositions of the depleted endmember in our mixing calculations (Figs 9 and 11a). The large variations of Nd–Hf isotope ratios in the pyroxenite samples cannot be explained by any known enriched mantle components (EM-I, EM-II, or HIMU) (Fig. 11a). It is possible that the enriched component contains a higher amount of ancient, recycled sediment or upper continental crust. To further investigate the nature of the enriched component in the mantle source of the Xiugugabu ophiolite, we plot Nd and Hf isotope ratios against selected trace element ratios in Fig. 12 (figures showing additional elemental ratios are presented in Appendix 8). In Fig. 12a and c, the negative correlations between Nd isotope ratios and La/Nd or Th/Nd suggest a mixing relationship between two components: one is the melt derived from partial melting of residual peridotite with DMM isotopic feature and the other is the enriched melt derived from a mantle source with high La/Nd and Th/Nd ratios. Similar conclusion can be drawn from initial Hf isotope ratios vs La/Hf, Th/Hf, Zr/Hf, and Sm/Hf ratios (Fig. 12b and d–f). A potential candidate for the enriched component that has high Zr/Hf ratios and low Sm/Hf ratios could be zircon-bearing, incompatible element-enriched sediment (e.g., Leat et al., 2004; Barry et al., 2006; Chauvel et al., 2008). In the absence of additional information, here, we choose the enriched component with the least radiogenic composition from ancient Himalaya sediments (<sup>143</sup>Nd/<sup>144</sup>Nd = 0.511348 and <sup>176</sup>Hf/<sup>177</sup>Hf = 0.281371; Richards et al., 2005) and trace element compositions from GLOSS-II (Plank, 2014). Before entering the peridotite melting region, the sediments must have melted and subsequently reacted with their surrounding depleted mantle. As a proof-of-concept, we use a mixture of 1% sediments and 99%

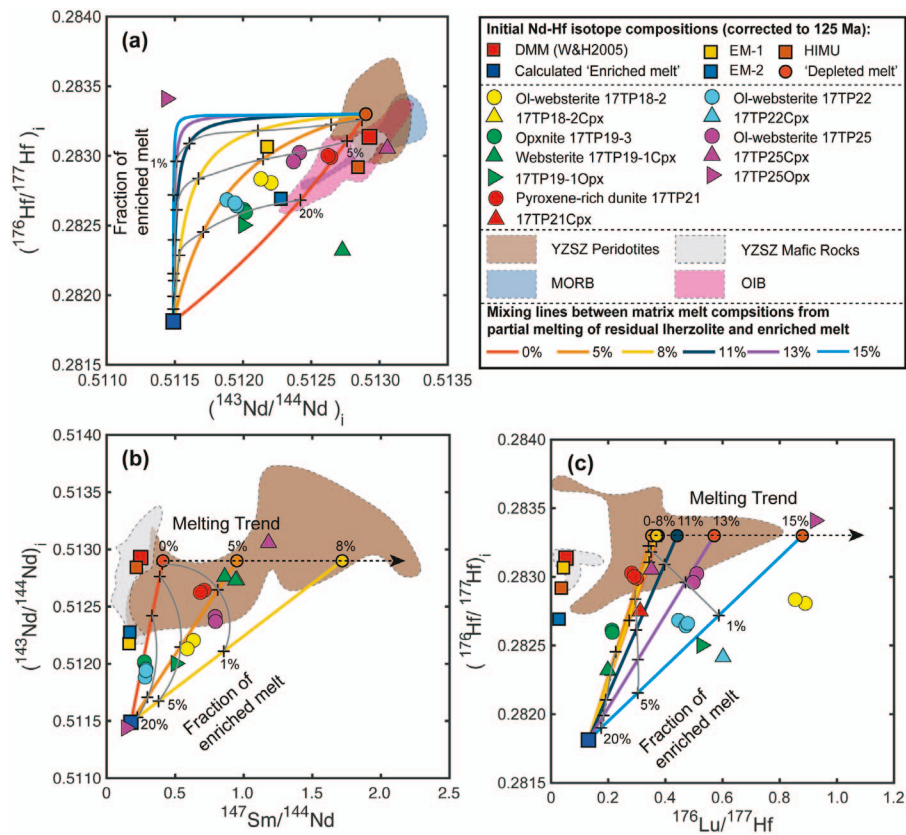


**Fig. 11.** Initial Nd–Hf isotopic compositions for the Xiugugabu pyroxenites and pyroxene-bearing dunite at 125 Ma. Binary mixing lines derived from mixing of matrix melt from residual peridotite and aggregated channel melt from the enriched mantle are shown as thick color-coded lines. The thin lines with plus symbols represent mixing lines for 0.1% to 20% enriched melt proportion. OIB and MORB compilations are from [Salters et al., 2011](#), and [Stracke et al., 2003](#). Source for compositions of YSZ peridotites and mafic rocks are the same as those listed in the caption to [Fig. 9](#).

residual lherzolite (sample 09-ZH-51 of [Bezard et al., 2011](#)) to simulate the enriched mantle composition in the modeling below. Both Nd–Hf isotope ratios of the sediment and the residual lherzolite is corrected to 125 Ma. [Figure 11](#) shows results of simple binary mixing calculations (heavy solid lines). In our model, the enriched endmember is the aggregated melt derived from 2% to 10% melting of the enriched mantle at a greater depth, and the depleted endmember is the instantaneous melt derived from 0% to 10% near fractional melting of the residual lherzolite that is near the pyroxenite veins from below ([Fig. 11](#)). Parameters used in the melting and mixing calculations are listed in [Table S5](#). Two main observations are summarized below.

Firstly, simple binary mixing between melts derived from the depleted mantle source and the enriched mantle source can explain most of the observed variations in  $(^{176}\text{Hf}/^{177}\text{Hf})_i - (^{143}\text{Nd}/^{144}\text{Nd})_i$ ,  $^{147}\text{Sm}/^{144}\text{Nd} - (^{143}\text{Nd}/^{144}\text{Nd})_i$ , and  $^{176}\text{Lu}/^{177}\text{Hf} - (^{176}\text{Hf}/^{177}\text{Hf})_i$  correlation diagrams ([Fig. 11](#)). Contributions of the enriched and depleted mantle to the pyroxenite depend on the assumption about trace element and isotopic compositions of the two endmembers and their degrees of melting. For example, at a given enriched melt composition, increasing the degree of melting of the depleted mantle would reduce the fraction of enriched mantle needed in the mantle source. [Figure 11](#) shows

that less than 20% enriched mantle derived melts are needed to explain the observed Nd–Hf isotope variations of the Xiugugabu pyroxenites. In more complicated mixing models that consider the size and lithology of the enriched mantle, larger variations in Nd–Hf isotope ratios are expected in the mixed melts (e.g., [Liu & Liang, 2017, 2020](#); [Liang, 2020](#)). Therefore, the 20% melts derived from the enriched mantle should be considered as an upper bound.

Secondly, initial Nd–Hf isotope compositions of clinopyroxene and orthopyroxene in two samples (17TP25 and 17TP19-1) are distinct and fall outside the mixing curves shown in [Fig. 11a](#). In the olivine websterite 17TP25, clinopyroxene has similar initial Nd–Hf isotope compositions to the age-corrected DMM, whereas orthopyroxene has a more refractory Hf isotope but an enriched Nd isotope composition ([Fig. 11a](#)). In composite pyroxenite vein 17TP19, the whole-rock Nd–Hf isotope composition of orthopyroxenite (17TP19-3) resemble those of orthopyroxene in the websterite (17TP19-1), whereas the clinopyroxene in this websterite sample has a more depleted initial Nd isotope composition than that in the bulk rock or orthopyroxene. It is likely that clinopyroxene and orthopyroxene in these pyroxenites were crystallized from different batches of melt. This is supported by major element compositions of the orthopyroxene and clinopyroxene discussed in

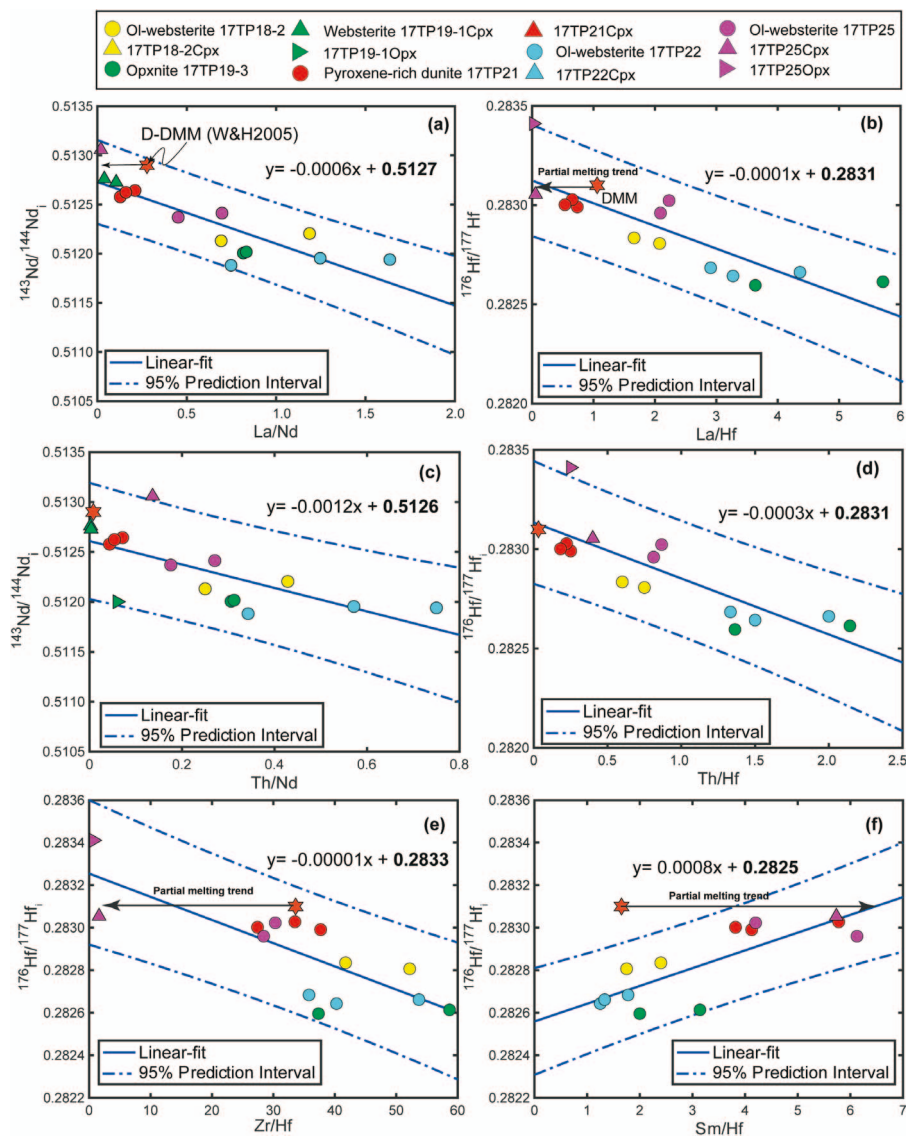


**Fig. 12.** Initial Nd-Hf isotopic composition vs trace element ratios: (a)  $^{143}\text{Nd}/^{144}\text{Nd}_i$  vs La/Nd; (b)  $^{176}\text{Hf}/^{177}\text{Hf}_i$  vs La/Hf; (c)  $^{143}\text{Nd}/^{144}\text{Nd}_i$  vs Th/Nd; (d)  $^{176}\text{Hf}/^{177}\text{Hf}_i$  vs Th/Hf; (e)  $^{176}\text{Hf}/^{177}\text{Hf}_i$  vs Zr/Hf; (f)  $^{176}\text{Hf}/^{177}\text{Hf}_i$  vs Sm/Hf. Solid lines are from linear regressions and dashed lines are the prediction interval of 95%. See text for discussion.

the preceding section. These hydrous melts were derived from partial melting of a hybrid mantle source including a DMM and a DMM metasomatized by ancient, recycled sediments. Finally, it is possible that the enriched component has lower  $^{176}\text{Hf}/^{177}\text{Hf}$  and higher  $^{143}\text{Nd}/^{144}\text{Nd}$  than that used in our modeling, which could better explain the Nd-Hf isotope ratios of the clinopyroxene samples.

### Trace element constraints on characteristics of infiltrating melts

To further examine the enriched and depleted mantle components identified by the Nd and Hf isotope ratios, we consider REE, Sr, Nb, Zr, Hf, and Ti concentrations in melts in equilibrium with the pyroxenites. The effect of subsolidus re-distribution on REE, Zr, Hf, and Ti between clinopyroxene and orthopyroxene is neglected in the modeling described below as a 200°C temperature

reduction (from 1300°C to 1100°C) would result in less than a factor of two variations in REE concentrations in the pyroxenes (for details, see Appendix 7). We use trace element concentrations in clinopyroxene and orthopyroxene in the pyroxenites and their partition coefficients to infer compositions of parental melts from which the pyroxenes were crystallized. The clinopyroxene-melt and orthopyroxene-melt partition coefficients were calculated using the parameterized lattice strain models for REE, Zr, Hf, and Ti (Sun & Liang, 2012, 2013; Yao et al., 2012; Sun, 2014), major element compositions of pyroxenes in the pyroxenite, and at a temperature of 1250°C. Partition coefficients for Nb and Sr are from (Kelemen et al., 2003). Partition coefficients used in this study were listed in Table S5.

Figure 13a and b shows N-MORB normalized trace element patterns of calculated melts in equilibrium with pyroxenitic clinopyroxene and orthopyroxene. In

general, the equilibrium melts are more depleted than mafic rocks that intruded into the Xiugugabu peridotites (Fig. 13c) (Bezard *et al.*, 2011; Zhong *et al.*, 2019). HREE in the calculated melts have higher concentrations and follow a different trend in the spider diagram than both high-Ca and low-Ca boninites (Fig. 13d) (Reagan *et al.*, 2010; Ishizuka *et al.*, 2011; Cluzel *et al.*, 2016; Woelki *et al.*, 2018). LREE, Sr, Nb, Zr, and Ti in the calculated melts in equilibrium with pyroxenitic orthopyroxene are higher than those in equilibrium with pyroxenitic clinopyroxene, whereas heavy to MREE in the calculated melts in equilibrium with pyroxenitic clinopyroxene are slightly higher than those in equilibrium with orthopyroxene (Fig. 13a and b). A striking feature of the melts in equilibrium with pyroxenitic clinopyroxene is the strong negative Zr anomaly and moderate negative Hf anomaly relative to Nd and Sm. The negative Zr and Hf anomalies were also observed in mafic rocks in the studied region (Fig. 13c) (Bezard *et al.*, 2011; Zhong *et al.*, 2019), although the amplitudes are smaller. We infer that the parental melts of the Xiugugabu pyroxenites were mixtures of melts generated by re-melting of the depleted peridotites and altered sediments. This is consistent with the initial Nd–Hf isotopic compositions of the Xiugugabu pyroxenites that show the mixing relationships between DMM-like YZSZ peridotites and ancient sediments (Figs 11 and 12). The contrasting trace element patterns between the calculated melts in equilibrium with pyroxenitic orthopyroxene and clinopyroxene (Fig. 13a and b) may result from early crystallization of orthopyroxene, followed by addition of an LREE- and Zr-depleted melt derived from peridotites in the underlying mantle.

To test the above hypothesis, we used a two-porosity melting model similar to the one described in Liang & Peng (2010) to calculate trace element patterns in the instantaneous melt produced by partial melting of a depleted and enriched lherzolite (called matrix melt hereafter) and the aggregated melt extracted to dunite channels (called channel melt). The trace element concentrations of the depleted lherzolite are from sample 09-ZH-51 of Bezard *et al.* (2011) that has the lowest Cr# in spinel and highest bulk REE contents (Fig. S3c in Appendix 2). The trace element concentrations of the enriched lherzolite are obtained by adding 1% of the alerted sediment GLOSS-II (Johnson & Plank, 1999; Plank, 2014) to the depleted lherzolite and (red squares in Fig. 14a and c). This choice of the enriched component is not unique (e.g., Stracke *et al.*, 2003) but adequate to demonstrate the basic idea here. Melting parameters used in the modeling are listed in Table S5. Figure 14a–d displays calculated trace element concentrations in the matrix melts and channel melts produced by 0%–10% near fractional melting of the two starting compositions. The channel melts have trace element patterns broadly similar to the calculated melts in equilibrium with pyroxenitic orthopyroxene (Fig. 14b and d).

The trace element patterns of clinopyroxene-derived melt could be produced by partly aggregating melts

from a more depleted mantle source (Fig. 14e and f). The higher Nb in the calculated melts may be attributed to the higher Nb concentrations in the enriched mantle sources than used in our modeling. The negative Zr and Hf anomalies in the calculated melts in equilibrium with clinopyroxene could be explained by (1) a starting lherzolite with more depleted Zr and Hf abundances (Fig. 7c), (2) presence of zircon in the residual mantle (Fig. 12e), or (3) disequilibrium melting of the starting lherzolite. Hydrous melting at low temperatures favors disequilibrium melting. Due to their slow diffusion rates in clinopyroxene and orthopyroxene (Bloch & Ganguly, 2014; D. Cherniak, pers. comm., 2021), Zr and Hf are less depleted in residual clinopyroxene and orthopyroxene during disequilibrium melting. Consequently, the channel melts are more depleted in Zr and Hf than the case of equilibrium melting (e.g., Liang & Liu, 2016).

In summary, our trace element modeling suggests that orthopyroxene and clinopyroxene in the Xiugugabu pyroxenites crystallized from different batches of melts. The parental melt of orthopyroxene is enriched in highly incompatible trace elements, whereas the parental melt of clinopyroxene is less enriched and has a large component of melt derived from partial melting of peridotites in the underlying mantle. Crystallization of different melt batches in the pyroxenite veins also provide a simple explanation to the observed differences in initial Nd and Hf isotope ratios between clinopyroxene and orthopyroxene in the websterite samples 17TP19 and 17TP25 (Fig. 11a) and Y and other trace element concentration profiles across the veins (Fig. 8; Appendix 3).

### Petrogenetic model for the Xiugugabu pyroxenites

The field occurrence and textures of the Xiugugabu pyroxenites are very similar to those observed in pyroxenites from the Bay of Islands ophiolite and the Voykar ophiolite (Varfalvy *et al.*, 1996; Suhr *et al.*, 2003; Batanova *et al.*, 2011; Belousov *et al.*, 2021), which were attributed to hydrous melt-peridotite reactions. Numerical simulations of dunite channel formation in a deformable harzburgite have shown that compaction in the central part of the dunite and dissolution of harzburgite at the dunite-harzburgite interface forced melt to localize along the harzburgite-dunite interface in the dunite side of the high-porosity channel (Liang *et al.*, 2010; Schiemenz *et al.*, 2011). At the lithosphere–asthenosphere boundary, the localized interstitial melt in the dunite channel starts to freeze (e.g., Morgan *et al.*, 2008; Rampone & Borghini, 2008; Dygert *et al.*, 2016; Basch *et al.*, 2019). Depending on melt flux from below, crystallization of the interstitial melt can lead to local pressure buildup, which in turn may induce higher porosity or hydro-fracture in the downstream direction in the dunite (Liang *et al.*, 2010; Schiemenz *et al.*, 2011). The accumulated melt in the high porosity melt vein may further react with its surrounding harzburgite and may even induce local fluxed melting of the host

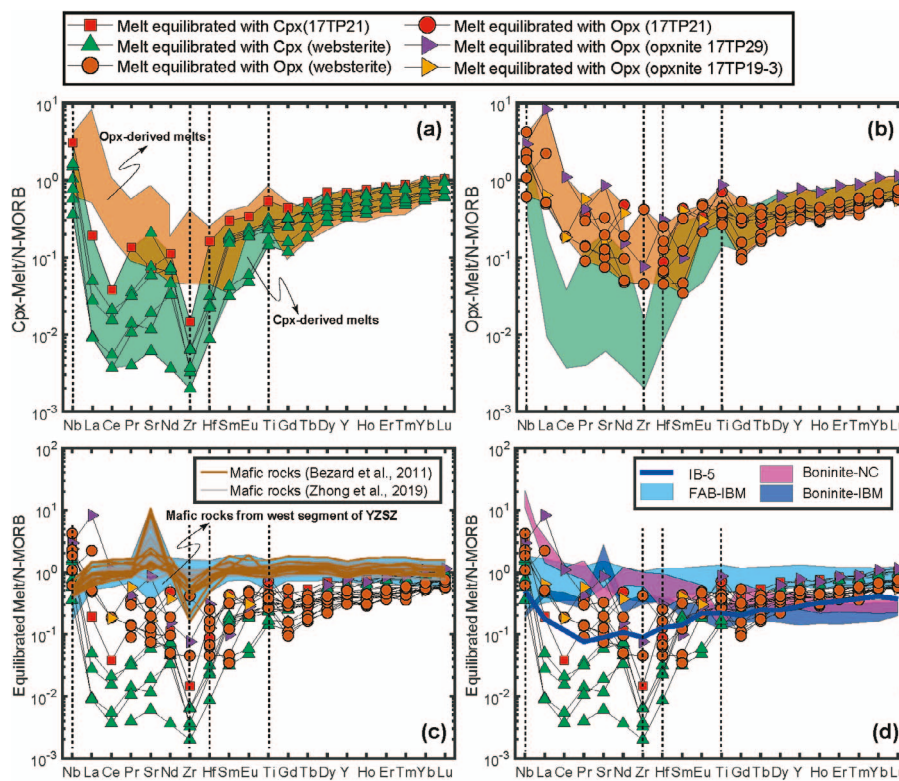


**Fig. 13.** (a, b) N-MORB (Sun & McDonough, 1989) normalized trace element compositions of melt in equilibrium with pyroxenitic clinopyroxene and orthopyroxene from the Xiugugabu ophiolite. (c, d) Mafic rocks from west segment of the YZSZ are compiled from Bezard *et al.*, 2011, Liu *et al.*, 2018a, and Zhong *et al.*, 2019. Forearc basalts and boninites from the Izu–Bonin–Mariana arc (Woodland *et al.*, 2002; Ishizuka *et al.*, 2011), boninites from the Troodos ophiolite (Woelki *et al.*, 2018), and boninites from the New Caledonia ophiolite (Cluzel *et al.*, 2016) are shown for comparison.

peridotite if the melt is hydrous and water in the melt diffuses into the surrounding harzburgite (Wang *et al.*, 2016b). Continuous cooling and crystallization of the melt vein could lead to the formation of trails of pyroxene megacrysts and/or pyroxenite veins in the dunite (Fig. 15a). The spatial distribution of the veins follows the melt distribution in the dunite channel. We envision that the Xiugugabu dunite was formed by reactive dissolution involving a hydrous melt during its transport through the partially molten peridotite in the asthenospheric mantle. This is supported by the nonlinear geometry of the composite dunite–pyroxenite veins (Fig. 3; Appendix 1) and the strike of the Xiugugabu pyroxenite veins that is parallel to the foliations of the host peridotites (Fig. 2a–c). The former indicates that the strong chemical exchange between pyroxenite veins and host peridotites and the latter indicates that melt flow occurred parallel to layering. Such features are typical of the Oman dunites and pyroxenites, which were originally formed in the asthenospheric mantle (Braun & Kelemen, 2002; Python & Ceuleneer, 2003). In addition, the systematic decrease in spinel grain size from the central dunite vein to the pyroxenite veins and host harzburgite (Fig. 3; Appendix 1) is likely produced by spinel partial dissolution during melt–peridotite reaction (Liang, 2003; Morgan *et al.*, 2008). In an upwelling mantle column, the dunite formed in the deeper part of the mantle would be eventually brought to

the lithosphere–asthenosphere boundary where freezing or crystallization commenced (e.g., Braun & Kelemen, 2002). When a late stage, hydrous- and silica-rich melt approached the lithosphere–asthenosphere boundary, reaction between the hydrous melt and peridotite would produce orthopyroxenites at the interface between dunite and host peridotite (Fig. 15a). A laboratory example of dunite–orthopyroxenite–harzburgite sequence formed by hydrous melt and peridotite interaction was reported by Wang *et al.* (2016b). When water-induced flux melting is extensive in the surrounding peridotite, the partial melt would flow along the local pressure gradient, accumulating and freezing on the newly formed orthopyroxenite, producing a dunite–orthopyroxenite–websterite vein sequence in the dunite (Fig. 15b). The dunite in between the websterite and harzburgite would be orthopyroxene-bearing, whereas the dunite in the center could be orthopyroxene-free (Fig. 15).

### Tectonic implications for the YZSZ

Ophiolites along the YZSZ are generally taken as relics of the Neo-Tethys Ocean and tectonic settings from which they were originated remain equivocal. Early studies have suggested that the YZSZ ophiolites were generated at slow-spreading ridges (e.g., Nicolas *et al.*, 1981), whereas later studies have proposed SSZ settings based on geochemical compositions of mafic rocks and/or mantle peridotites, either in a forearc (e.g.,

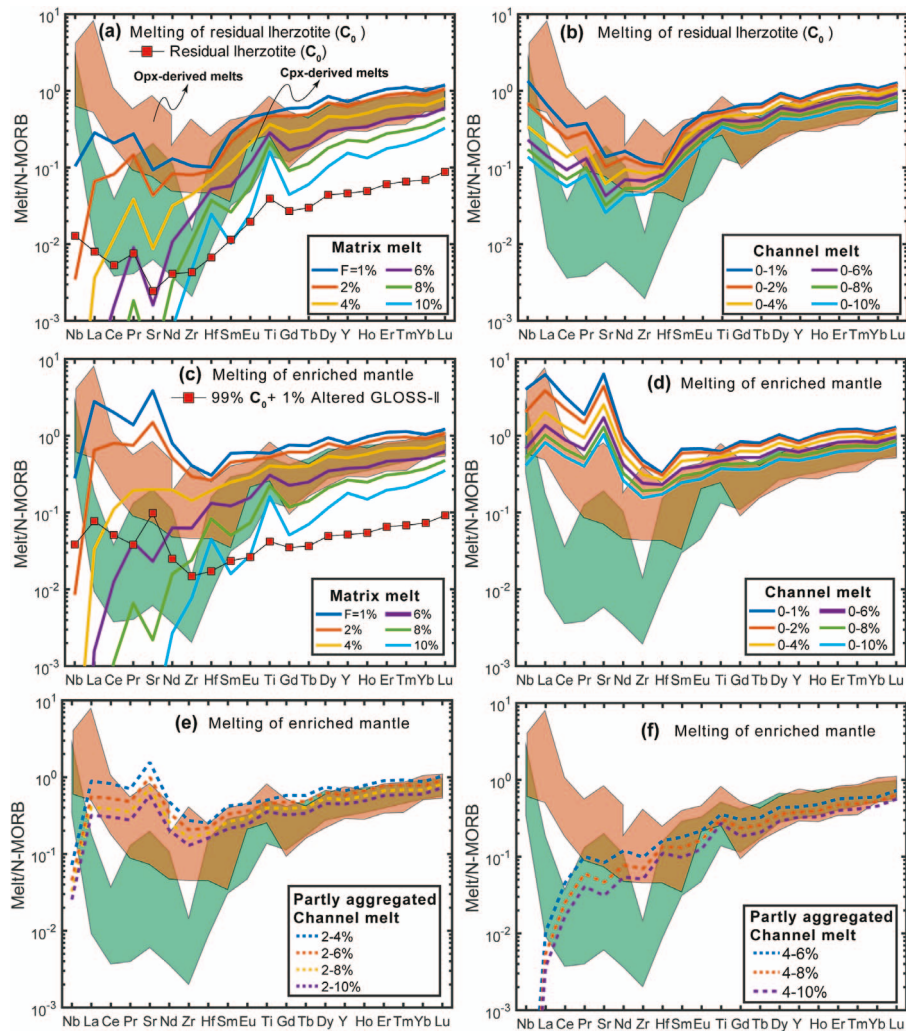


**Fig. 14.** Trace element patterns of matrix melt and channel melt derived from partial melting of the Xiugugabu residual lherzolite. Trace element concentrations are normalized to N-MORB (Sun & McDonough, 1989). (a) Trace element concentrations of matrix melts (lines) calculated from re-melting of a residual lherzolite. (b) The thick lines represent trace element patterns of aggregated melts. (c, d) Similar to (a, b) but the trace element concentrations in the starting lherzolite contains 1% altered sediments. (e, f) Similar to (d) but only partly aggregate matrix melt from 2% to 4% melting, 4% to 6% melting, etc. See text for discussion.

Dai et al., 2013; Maffione et al., 2015; Xiong et al., 2016) or a back-arc setting (e.g., Guilmette et al., 2012). More recent studies have invoked that the YZSZ ophiolites represent oceanic core complexes generated at ultraslow spreading ridges (Liu et al., 2014, 2021; Zhang et al., 2019).

The Xiugugabu dunites have low spinel Cr# values that are comparable to those previously reported for dunitic spinel (e.g., Xiong et al., 2017a, 2017c), which supports the inference that the Xiugugabu dunites were formed via the reaction between a silica-unsaturated melt (i.e., MORB-like) and mantle peridotite. Here, we have shown that the Xiugugabu pyroxenite veins represent the crystallization of hydrous and silica-enriched melts with unradiogenic Nd–Hf isotope compositions in a partially molten mantle, near the lithosphere–asthenosphere boundary. Therefore, the Xiugugabu pyroxenites and dunite witness the transition of tectonic settings from MOR to SSZ.

Such a transition can be explained by either the subduction initiation model (e.g., Dai et al., 2013, 2021; Xiong

et al., 2016, 2017b, 2017c) or the subduction re-initiation model (Zhang et al., 2019; Liu et al., 2022). According to the subduction re-initiation model, the YZSZ ophiolites represent relics of oceanic core complex generated at ultraslow spreading ridges and clogged at the trench, which triggered re-initiation of a new subduction in the south flank of the Neo-Tethys Ocean. Although the subduction initiation model cannot be completely ruled out, here, we prefer the subduction re-initiation model for the following considerations. Firstly, mantle peridotites from the Xiugugabu ophiolite have compositions more fertile (e.g., low spinel Cr# and higher contents of  $\text{Al}_2\text{O}_3$  and REE in clinopyroxene) than typical forearc peridotites (Appendix 2), which argues against high-degrees of melting in a SSZ setting. Secondly, gabbroic intrusions in the Xiugugabu peridotites have flat REE patterns (Fig. 11c) and depleted Nd–Hf isotopes (Fig. 13b and c), which are geochemically similar to present-day MORB (Bezard et al., 2011; Zhong et al., 2019). Finally, a recent study on gabbros of the Xigaze ophiolite in the central segment of

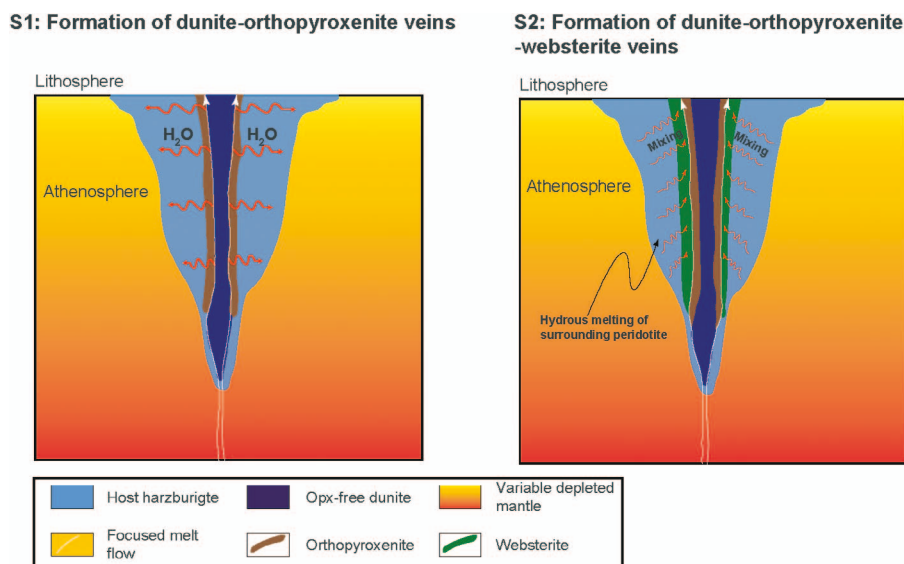


**Fig. 15.** Schematic diagram illustrating the formation of composite dunite–orthopyroxenite–websterite veins. (S1) Formation of orthopyroxenite at the boundary between dunite and host peridotite during percolation of a hydrous-, silica-rich melt in the dunite channel. Diffusional loss of water from the hydrous melt to surrounding peridotite causes re-melting of surrounding peridotite forming a depleted melt. (S2) Reactive crystallization of the depleted melt forms the websterite at the boundary between orthopyroxenite and host peridotite. See text for discussion.

the YZSZ revealed an episodic and intermittent magma supply within the lower oceanic crust, a feature that is only observed in present-day ultraslow spreading ridges (Liu *et al.*, 2021).

Therefore, we proposed that the Xiugugabu ophiolite was generated at an ultraslow spreading ridge as an ocean core complex (OCC), which was very close to the southern margin of the Lhasa terrane according to paleomagnetism data (Huang *et al.*, 2015; Li *et al.*, 2016). Asthenosphere-derived MORB-like magmas were transported in the oceanic mantle and reaction with the host peridotites produced the Xiugugabu dunite veins. Shortly after its formation, the Xiugugabu OCC entered the subduction zone and clogged in the trench, due to its high topography. This would result in the demise of an old subduction zone and northward drifting of the Indian continent exerted a far-field compressional strength, which initiated a new subduction in the south of the clogged OCC. Sediments were subducted along with the new subduction and recycled to metasomatize the mantle. Partial melting of such metasomatized mantle sources would give rise to enriched melts required by the formation of the Xiugugabu pyroxenites.

## CONCLUSION

The Xiugugabu pyroxenite veins are crystallization products of hybrid hydrous melts formed at the waning stage of partial melting and reactive melt transport in the asthenospheric mantle. Results from this study enable us to develop a model for the formation of composite dunite-pyroxenite veins in residual peridotite. The model has four key components or steps. (1) Re-melting of previous depleted mantle forms hydrous, silica-saturated, and incompatible trace element-depleted melt. (2)

Percolation of the hydrous melt through the dunite channel results in reactive dissolution of the surrounding peridotite and formation of the orthopyroxenite at the interface between the dunite and host peridotite. (3) Diffusional loss of water from the hydrous melt in the dunite channel induces partial melting of the surrounding residual peridotite, producing hybrid melts that are depleted in highly incompatible trace elements. (4) The hybrid melt would flow along the local pressure gradient, crystallizing on the newly formed orthopyroxenite, forming the composite dunite–orthopyroxenite–websterite vein sequence. Such a mechanism can also explain the coexistence of pyroxenites and dunites in the mantle sections of other ophiolites around the world (Suhr *et al.*, 2003; Tamura & Arai, 2006; Batanova *et al.*, 2011; Sergeev *et al.*, 2014; Kaczmarek *et al.*, 2015).

The present study has demonstrated the advantages of studying trace element and isotope compositions in coexisting clinopyroxene and orthopyroxene in the pyroxenites. Distinct trace element patterns between clinopyroxene- and orthopyroxene-derived melts and different Nd–Hf isotope compositions of clinopyroxene and orthopyroxene within each sample in the Xiugugabu pyroxenite veins have provided strong evidence for the crystallization of the pyroxenes from different batches of melts. The parental melt of orthopyroxene is more enriched in incompatible trace elements and Nd–Hf isotope compositions than the parental melt of clinopyroxene. The latter has a larger contribution of melt derived from re-melting of previously depleted peridotite in the underlying mantle. The extremely enriched Nd–Hf isotope compositions of the Xiugugabu pyroxenite veins reveal that the mantle source of the Xiugugabu ophiolite is considerably more heterogeneous, which can be explained by the existence of ancient and

recycled sediments or upper continental crusts. Melting of such a heterogeneous mantle can produce melts with spoon-shaped trace element patterns similar to those observed in the Xiugugabu pyroxenites and the peridotites from the YZSZ (Fig. 13; Appendix 2).

The magmatic sequences recorded within the Xiugugabu ophiolite are 'MORB' melts followed by hydrous and highly incompatible element-enriched melts. Considering low degrees of melting experienced by the co-existing mantle peridotites, results from the Xiugugabu pyroxenites provide supports to the subduction re-initiation model, i.e., the Xiugugabu was formed as OCC in an ultraslow spreading ridge, which was subsequently clogged in the trench and had triggered a new subduction.

## SUPPLEMENTARY DATA

Supplementary data are available at *Journal of Petrology* online.

## FUNDING

This study was supported by grants from the National Science Fund for Distinguished Young Scholars (42025201); the National Key Research and Development Project of China (2020YFA0714801); and the US National Science Foundation (OCE-1852088).

## CONFLICT OF INTEREST STATEMENT

All authors disclosed no relevant relationships.

## ACKNOWLEDGEMENTS

We are indebted to Shitou Wu, Yueheng Yang, Chao Huang, and Di Zhang for their help during data acquisition. Many stimulating conversations have been had with Henry Dick on the nature of pyroxenite veins. We thank Jason Harvey and Qing Xiong for their constructive reviews and Jason Harvey and Georg Zellmer for their editorial handling. Zhenyu Zhang thanks the UCAS Joint PhD Training Program for providing the opportunity to visit the Brown University.

## References

- Allègre, C. J. & Turcotte, D. L. (1986). Implications of a two-component marble-cake mantle. *Nature* **323**, 123–127.
- An, W., Hu, X., Garzanti, E., BouDagher-Fadel, M. K., Wang, J. & Sun, G. (2014). Xigaze forearc basin revisited (South Tibet): provenance changes and origin of the Xigaze ophiolite. *Geological Society of America Bulletin* **126**, 1595–1613.
- Anders, E. & Grevesse, N. (1989). Abundances of the elements: meteoritic and solar. *Geochimica et Cosmochimica Acta* **53**, 197–214.
- Asimow, P. D. & Ghiorso, M. S. (1998). Algorithmic modifications extending MELTS to calculate subsolidus phase relations. *American Mineralogist* **83**, 1127–1132.
- Barry, T. L., Pearce, J. A., Leat, P. T., Millar, I. L. & le Roex, A. P. (2006). Hf isotope evidence for selective mobility of high-field-strength elements in a subduction setting: South Sandwich Islands. *Earth and Planetary Science Letters* **252**, 223–244.
- Basch, V., Rampone, E., Borghini, G., Ferrando, C. & Zanetti, A. (2019). Origin of pyroxenites in the oceanic mantle and their implications on the reactive percolation of depleted melts. *Contributions to Mineralogy and Petrology* **174**, 97. <https://doi.org/10.1007/s00410-019-1640-0>.
- Batanova, V. G., Belousov, I. A., Savelieva, G. N. & Sobolev, A. V. (2011). Consequences of channelized and diffuse melt transport in supra-subduction zone mantle: evidence from the Voykar ophiolite (Polar Urals). *Journal of Petrology* **52**, 2483–2521.
- Belousov, I., Batanova, V., Sobolev, A., Savelieva, G., Danyushevsky, L. & Draayers, E. (2021). Pyroxenites from mantle section of Voykar ophiolite—melt/peridotite reaction and crystallization in SSZ mantle. *Lithos* **388–389**, 106063.
- Bénard, A., Le Losq, C., Nebel, O. & Arculus, R. J. (2018). Low-Ca boninite formation by second-stage melting of spinel harzburgite residues at mature subduction zones: new evidence from veined mantle xenoliths from the West Bismarck arc. *Contributions to Mineralogy and Petrology* **173**, 105.
- Bezard, R., Hébert, R., Wang, C., Dostal, J., Dai, J. & Zhong, H. (2011). Petrology and geochemistry of the Xiugugabu ophiolitic massif, western Yarlung Zangbo suture zone, Tibet. *Lithos* **125**, 347–367.
- Bloch, E. & Ganguly, J. (2014).  $^{176}\text{Lu}$ – $^{176}\text{Hf}$  and  $^{147}\text{Sm}$ – $^{143}\text{Nd}$  ages of the Martian shergottites: evaluation of the shock-resetting hypothesis through diffusion kinetic experiments and modeling, and petrological observations. *Earth and Planetary Science Letters* **395**, 173–183.
- Bodinier, J. L. & Godard, M. (2014). Orogenic, ophiolitic, and abyssal peridotites. In: (Holland H. D. & Turekian K. K. (eds)) *Treatise on Geochemistry*, vol. 3, 2nd edn. Oxford: Elsevier, pp.103–167. <https://doi.org/10.1016/B978-0-08-095975-7.00204-7>.
- Bodinier, J., Guiraud, M., Fabries, J., Dostal, J. & Dupuy, C. (1987). Petrogenesis of layered pyroxenites from the Lherz, Freychinede and Prades ultramafic bodies (Ariege, French Pyrenees). *Geochimica et Cosmochimica Acta* **51**, 279–290.
- Bodinier, J. L., Garrido, C. J., Chanefo, I., Bruguier, O. & Gervilla, F. (2008). Origin of pyroxenite-peridotite veined mantle by refertilization reactions: evidence from the Ronda peridotite (southern Spain). *Journal of Petrology* **49**, 999–1025.
- Borghini, G., Fumagalli, P. & Rampone, E. (2010). The stability of plagioclase in the upper mantle: subsolidus experiments on fertile and depleted lherzolite. *Journal of Petrology* **51**, 229–254.
- Borghini, G., Rampone, E., Zanetti, A., Class, C., Cipriani, A., Hofmann, A. W. & Goldstein, S. L. (2013). Meter-scale Nd isotopic heterogeneity in pyroxenite-bearing Ligurian peridotites encompasses global-scale upper mantle variability. *Geology* **41**, 1055–1058.
- Borghini, G., Rampone, E., Zanetti, A., Class, C., Cipriani, A., Hofmann, A. W. & Goldstein, S. L. (2016). Pyroxenite layers in the northern Apennines' upper mantle (Italy)—generation by pyroxenite melting and melt infiltration. *Journal of Petrology* **57**, 625–653.
- Bouvier, A., Vervoort, J. D. & Patchett, P. J. (2008). The Lu–Hf and Sm–Nd isotopic composition of CHUR: constraints from unequilibrated chondrites and implications for the bulk composition of terrestrial planets. *Earth and Planetary Science Letters* **273**, 48–57.
- Braun, M. G. & Kelemen, P. B. (2002). Dunite distribution in the Oman ophiolite: implications for melt flux through porous dunite conduits. *Geochemistry, Geophysics, Geosystems* **3**, 1–21.
- Brey, G. P. & Köhler, T. (1990). Geothermobarometry in four-phase lherzolites II. New thermobarometers, and practical assessment of existing thermobarometers. *Journal of Petrology* **31**, 1353–1378.

- Cannat, M., Sauter, D., Mendel, V., Ruellan, E., Okino, K., Escartin, J., Combiér, V. & Baala, M. (2006). Modes of seafloor generation at a melt-poor ultraslow-spreading ridge. *Geology* **34**, 605–608.
- Chauvel, C., Lewin, E., Carpentier, M., Arndt, N. T. & Marini, J.-C. (2008). Role of recycled oceanic basalt and sediment in generating the Hf–Nd mantle array. *Nature Geoscience* **1**, 64–67.
- Chen, L.-H. & Zhou, X.-H. (2005). Subduction-related metasomatism in the thinning lithosphere: evidence from a composite dunite-orthopyroxenite xenolith entrained in Mesozoic Laiwu high-Mg diorite, North China Craton. *Geochemistry, Geophysics, Geosystems* **6**, Q06008.
- Cheng, X., Xia, B., Li, J., Yu, M., Zhong, L., Huang, Q. & Shi, Q. (2011). Sr–Nd–Pb isotopic characteristics and origin of the mantle peridotites from the Luobusha ophiolite. *Geotectonica et Metallogenia* **35**, 85–94.
- Cheng, C., Xia, B., Zheng, H., Yuan, Y., Yin, Z., Lu, Y. & Zhang, X. (2018). Chronology, geochemistry and tectonic significance of Daba ophiolites in western segment of Yarlung Zangbo suture zone, Tibet. *Earth Science* **43**, 975–990.
- Cherniak, D. J. & Dimanov, A. (2010). Diffusion in pyroxene, mica and amphibole. *Reviews in Mineralogy and Geochemistry* **72**, 641–690.
- Chung, S.-L., Chu, M.-F., Zhang, Y., Xie, Y., Lo, C.-H., Lee, T.-Y., Lan, C.-Y., Li, X., Zhang, Q. & Wang, Y. (2005). Tibetan tectonic evolution inferred from spatial and temporal variations in post-collisional magmatism. *Earth-Science Reviews* **68**, 173–196.
- Cluzel, D., Ulrich, M., Jourdan, F., Meffre, S., Paquette, J.-L., Audet, M.-A., Secchiari, A. & Maurizot, P. (2016). Early Eocene clinostatite boninite and boninite-series dikes of the ophiolite of New Caledonia; a witness of slab-derived enrichment of the mantle wedge in a nascent volcanic arc. *Lithos* **260**, 429–442.
- Dai, J.-G., Wang, C., Polat, A., Santosh, M., Li, Y. & Ge, Y. (2013). Rapid forearc spreading between 130 and 120 Ma: evidence from geochronology and geochemistry of the Xigaze ophiolite, southern Tibet. *Lithos* **172–173**, 1–16.
- Dai, J.-G., Wang, C.-S., Stern, R. J., Yang, K. & Shen, J. (2021). Forearc magmatic evolution during subduction initiation: insights from an early cretaceous Tibetan ophiolite and comparison with the Izu–Bonin–Mariana forearc. *GSA Bulletin* **133**, 753–776.
- Dantas, C., Ceuleneer, G., Gregoire, M., Python, M., Frey, R., Warren, J. & Dick, H. J. B. (2007). Pyroxenites from the southwest Indian ridge, 9–16 E: cumulates from incremental melt fractions produced at the top of a cold melting regime. *Journal of Petrology* **48**, 647–660.
- Dantas, C., Grégoire, M., Koester, E., Conceição, R. V. & Rieck, N. (2009). The lherzolite–websterite xenolith suite from northern Patagonia (Argentina): evidence of mantle–melt reaction processes. *Lithos* **107**, 107–120.
- DePaolo, D. J. (1981). Neodymium isotopes in the Colorado front range and crust–mantle evolution in the Proterozoic. *Nature* **291**, 193–196.
- Dick, H. J. B., Lin, J. & Schouten, H. (2003). An ultraslow-spreading class of ocean ridge. *Nature* **426**, 405–412.
- Dick, H. J. B., Lissenberg, C. J. & Warren, J. M. (2010). Mantle melting, melt transport, and delivery beneath a slow-spreading ridge: the paleo-MAR from 23°15′ N to 23°45′ N. *Journal of Petrology* **51**, 425–467.
- Downes, H. (2007). Origin and significance of spinel and garnet pyroxenites in the shallow lithospheric mantle: ultramafic massifs in orogenic belts in Western Europe and NW Africa. *Lithos* **99**, 1–24.
- Dygert, N., Liang, Y. & Kelemen, P. B. (2016). Formation of plagioclase lherzolite and associated dunite–harzburgite–lherzolite sequences by multiple episodes of melt percolation and melt–rock reaction: an example from the trinity ophiolite, California, USA. *Journal of Petrology* **57**, 815–838.
- Dygert, N., Kelemen, P. B. & Liang, Y. (2017). Spatial variations in cooling rate in the mantle section of the Samail ophiolite in Oman: implications for formation of lithosphere at mid-ocean ridges. *Earth and Planetary Science Letters* **465**, 134–144.
- Elthon, D. & Scarfe, C. M. (1984). High-pressure phase equilibria of a high-magnesia basalt and the genesis of primary oceanic basalts. *American Mineralogist* **69**, 15.
- Falloon, T. J. & Danyushevsky, L. V. (2000). Melting of refractory mantle at 1.5, 2 and 2.5 GPa under anhydrous and H<sub>2</sub>O-undersaturated conditions: implications for the petrogenesis of high-Ca boninites and the influence of subduction components on mantle melting. *Journal of Petrology* **41**, 257–283.
- Frey, F. A. & Prinz, M. (1978). Ultramafic inclusions from San Carlos, Arizona: petrologic and geochemical data bearing on their petrogenesis. *Earth and Planetary Science Letters* **38**, 129–176.
- Garrido, C. J. & Bodinier, J. L. (1999). Diversity of mafic rocks in the Ronda peridotite: evidence for pervasive melt–rock reaction during heating of subcontinental lithosphere by upwelling asthenosphere. *Journal of Petrology* **40**, 729–754.
- Gasparik, T. (1984). Two-pyroxene thermobarometry with new experimental data in the system CaO–MgO–Al<sub>2</sub>O<sub>3</sub>–SiO<sub>2</sub>. *Contributions to Mineralogy and Petrology* **87**, 87–97.
- Ghiorso, M. S. & Sack, R. O. (1995). Chemical mass transfer in magmatic processes IV. A revised and internally consistent thermodynamic model for the interpolation and extrapolation of liquid–solid equilibria in magmatic systems at elevated temperatures and pressures. *Contributions to Mineralogy and Petrology* **119**, 197–212.
- Ghiorso, M. S., Hirschmann, M. M., Reiners, P. W. & Kress, V. C., I. I. I. (2002). The pMELTS: a revision of MELTS for improved calculation of phase relations and major element partitioning related to partial melting of the mantle to 3 GPa. *Geochemistry, Geophysics, Geosystems* **3**, 1–35.
- Girardeau, J., Mercier, J. C. C. & Xibin, W. (1985). Petrology of the mafic rocks of the Xigaze ophiolite, Tibet. *Contributions to Mineralogy and Petrology* **90**, 309–321.
- Gong, X.-H., Shi, R.-D., Griffin, W. L., Huang, Q.-S., Xiong, Q., Chen, S.-S., Zhang, M. & O'Reilly, S. Y. (2016). Recycling of ancient subduction-modified mantle domains in the Purang ophiolite (southwestern Tibet). *Lithos* **262**, 11–26.
- Gong, X. H., Shi, R. D., Xu, J. F., Huang, Q. S., Huang, X. X. & Su, B. X. (2020). “Garnet” lherzolites in the Purang ophiolite, Tibet: evidence for exhumation of deep oceanic lithospheric mantle. *Geophysical Research Letters* **47**, e2019GL086101.
- Green, D. H. & Ringwood, A. E. (1967). The genesis of basaltic magmas. *Contributions to Mineralogy and Petrology* **15**, 103–190.
- Grove, T. L., Chatterjee, N., Parman, S. W. & Médard, E. (2006). The influence of H<sub>2</sub>O on mantle wedge melting. *Earth and Planetary Science Letters* **249**, 74–89.
- Grove, T. L., Till, C. B. & Krawczynski, M. J. (2012). The role of H<sub>2</sub>O in subduction zone magmatism. *Annual Review of Earth and Planetary Sciences* **40**, 413–439.
- Guangwei, L., Xiaohan, L., Alex, P., Lijie, W., Xiaobing, L., Feixin, H. & Xuejun, Z. (2010). In-situ detrital zircon geochronology and Hf isotopic analyses from upper Triassic Tethys sequence strata. *Earth and Planetary Science Letters* **297**, 461–470.
- Guilmette, C., Hébert, R., Wang, C. & Villeneuve, M. (2009). Geochemistry and geochronology of the metamorphic sole underlying the Xigaze ophiolite, Yarlung Zangbo suture zone, South Tibet. *Lithos* **112**, 149–162.

- Guilmette, C., Hébert, R., Dostal, J., Indares, A., Ullrich, T., Bédard, É. & Wang, C. (2012). Discovery of a dismembered metamorphic sole in the Saga ophiolitic mélange, South Tibet: assessing an early cretaceous disruption of the Neo-Tethyan supra-subduction zone and consequences on basin closing. *Gondwana Research* **22**, 398–414.
- Guo, G., Yang, J., Liu, X., Xu, X., Liu, Z. & Ba, D. (2015). Mid-ocean ridge (MOR) and suprasubduction zone (SSZ) geological events in the Yarlung Zangbo suture zone: Evidence from the mineral record of mantle peridotites. *Journal of Asian Earth Sciences* **110**, 33–54.
- Gysi, A. P., Jagoutz, O., Schmidt, M. W. & Targuisti, K. (2011). Petrogenesis of pyroxenites and melt infiltrations in the ultramafic complex of Beni Bousera, northern Morocco. *Journal of Petrology* **52**, 1679–1735.
- Huang, W., van Hinsbergen, D. J. J., Maffione, M., Orme, D. A., Dupont-Nivet, G., Guilmette, C., Ding, L., Guo, Z. & Kapp, P. (2015). Lower cretaceous Xigaze ophiolites formed in the Gangdese forearc: evidence from paleomagnetism, sediment provenance, and stratigraphy. *Earth and Planetary Science Letters* **415**, 142–153.
- Ionov, D. A., Doucet, L. S., Xu, Y., Golovin, A. V. & Oleinikov, O. B. (2018). Reworking of Archean mantle in the NE Siberian craton by carbonatite and silicate melt metasomatism: evidence from a carbonate-bearing, dunite-to-websterite xenolith suite from the Obnazhennaya kimberlite. *Geochimica et Cosmochimica Acta* **224**, 132–153.
- Ishizuka, O., Tani, K., Reagan, M. K., Kanayama, K., Umino, S., Hari-gane, Y., Sakamoto, I., Miyajima, Y., Yuasa, M. & Dunkley, D. J. (2011). The timescales of subduction initiation and subsequent evolution of an oceanic island arc. *Earth and Planetary Science Letters* **306**, 229–240.
- Ji, W.-Q., Wu, F.-Y., Chung, S.-L., Li, J.-X. & Liu, C.-Z. (2009). Zircon U–Pb geochronology and Hf isotopic constraints on petrogenesis of the Gangdese batholith, southern Tibet. *Chemical Geology* **262**, 229–245.
- Ji, W.-Q., Wu, F.-Y., Chung, S.-L. & Liu, C.-Z. (2014). The Gangdese magmatic constraints on a latest Cretaceous lithospheric delamination of the Lhasa terrane, southern Tibet. *Lithos* **210–211**, 168–180.
- Johnson, M. C. & Plank, T. (1999). Dehydration and melting experiments constrain the fate of subducted sediments. *Geochemistry, Geophysics, Geosystems* **1**, 1007.
- Kaczmarek, M.-A., Jonda, L. & Davies, H. L. (2015). Evidence of melting, melt percolation and deformation in a supra-subduction zone (Marum ophiolite complex, Papua New Guinea). *Contributions to Mineralogy and Petrology* **170**, 19.
- Kelemen, P., Hirth, G., Shimizu, N., Spiegelman, M. & Dick, H. (1997). A review of melt migration processes in the adiabatically upwelling mantle beneath oceanic spreading ridges. *Philosophical Transactions of the Royal Society A* **355**, 283–318.
- Kelemen, P. B., Yogodzinski, G. M. & Scholl, D. W. (2003). Along-strike variation in the Aleutian Island arc: genesis of high Mg# andesite and implications for continental crust. *Inside the Subduction Factory* **138**, 223–276.
- Laukert, G., von der Handt, A., Hellebrand, E., Snow, J. E., Hoppe, P. & Klügel, A. (2014). High-pressure reactive melt stagnation recorded in abyssal pyroxenites from the ultraslow-spreading Lena Trough, Arctic Ocean. *Journal of Petrology* **55**, 427–458.
- Le Roux, V. & Liang, Y. (2019). Ophiolitic pyroxenites record boninite percolation in subduction zone mantle. *Minerals* **9**, 565.
- Le Roux, V., Dick, H. & Shimizu, N. (2014). Tracking flux melting and melt percolation in supra-subduction peridotites (Josephine ophiolite, USA). *Contributions to Mineralogy and Petrology* **168**, 1064.
- Leake, B. E., Woolley, A. R., Arps, C. E., Birch, W. D., Gilbert, M. C., Grice, J. D., Hawthorne, F. C., Kato, A., Kisch, H. J., Krivovichev, V. G., Linthout, K., Laird, J., Mandarino, J., Maresch, W. V., Nickel, E. H., Rock, N. M. S., Schumacher, J. C., Smith, D. C., Stephenson, N. C. N., Ungaretti, L., Whittaker, E. J. W. & Youzhi, G. (1997). Nomenclature of amphiboles; report of the subcommittee on amphiboles of the international mineralogical association commission on new minerals and mineral names. *Mineralogical Magazine* **61**, 295–310.
- Leat, P. T., Pearce, J. A., Barker, P. F., Millar, I. L., Barry, T. L. & Larter, R. D. (2004). Magma genesis and mantle flow at a subducting slab edge: the South Sandwich arc-basin system. *Earth and Planetary Science Letters* **227**, 17–35.
- Li, W.-X. (2013). Geochemical characteristics and tectonic environments of the Yarlung Zangbo ophiolites in Xigaze, Tibet. Ph.D. thesis (in Chinese with English abstract). 1–117. <https://kns.cnki.net/kcms/>.
- Li, Z., Ding, L., Lippert, P. C., Song, P., Yue, Y. & van Hinsbergen, D. J. J. (2016). Paleomagnetic constraints on the Mesozoic drift of the Lhasa terrane (Tibet) from Gondwana to Eurasia. *Geology* **44**, 727–730.
- Lian, D., Yang, J., Robinson, P. T., Liu, F., Xiong, F., Zhang, L., Gao, J. & Wu, W. (2016). Tectonic evolution of the Western Yarlung Zangbo Ophiolitic Belt, Tibet: implications from the petrology, mineralogy, and geochemistry of the peridotites. *The Journal of Geology* **124**, 353–376.
- Liang, Y. (2003). Kinetics of crystal-melt reaction in partially molten silicates: 1. Grain scale processes. *Geochemistry, Geophysics, Geosystems* **4**, 1045.
- Liang, Y. (2020). Trace element fractionation and isotope ratio variation during melting of a spatially distributed and lithologically heterogeneous mantle. *Earth and Planetary Science Letters* **552**, 116594.
- Liang, Y. & Liu, B. (2016). Simple models for disequilibrium fractional melting and batch melting with application to REE fractionation in abyssal peridotites. *Geochimica et Cosmochimica Acta* **173**, 181–197.
- Liang, Y. & Peng, Q. (2010). Non-modal melting in an upwelling mantle column: steady-state models with applications to REE depletion in abyssal peridotites and the dynamics of melt migration in the mantle. *Geochimica et Cosmochimica Acta* **74**, 321–339.
- Liang, Y., Schiemenz, A., Hesse, M. A., Parmentier, E. M. & Hesthaven, J. S. (2010). High-porosity channels for melt migration in the mantle: top is the dunite and bottom is the harzburgite and lherzolite. *Geophysical Research Letters* **37**, L15306.
- Liang, Y., Sun, C. & Yao, L. (2013). A REE-in-two-pyroxene thermometer for mafic and ultramafic rocks. *Geochimica et Cosmochimica Acta* **102**, 246–260.
- Liang, Y., Ji, Z. & Liu, B. (2021). What can we learn from REE abundances in clinopyroxene and orthopyroxene in residual mantle peridotites? *Contributions to Mineralogy and Petrology* **176**, 24.
- Liu, G. & Einsele, G. (1996). Various types of olistostromes in a closing ocean basin, Tethyan Himalaya (cretaceous, Tibet). *Sedimentary Geology* **104**, 203–226.
- Liu, G. & Einsele, G. (1999). Jurassic sedimentary facies and paleogeography of the former Indian passive margin in southern Tibet. In: (Macfarlane A., Sorkhabi R. & Quade J. (eds)) *Himalaya and Tibet: Mountain Root to Mountain Top*. Geological Society of America. Special Paper 328, pp. 75–108.
- Liu, B. & Liang, Y. (2017). The prevalence of kilometer-scale heterogeneity in the source region of MORB upper mantle. *Science Advances* **3**, e1701872.
- Liu, B. & Liang, Y. (2020). Importance of the size and distribution of chemical heterogeneities in the mantle source to the variations of isotope ratios and trace element abundances in mid-ocean ridge basalts. *Geochimica et Cosmochimica Acta* **268**, 383–404.

- Liu, Y., Gao, S., Lee, C. T. A., Hu, S., Liu, X. & Yuan, H. (2005). Melt-peridotite interactions: links between garnet pyroxenite and high-Mg# signature of continental crust, earth planet. *Earth & Planetary Science Letters* **234**, 39–57.
- Liu, C.-Z., Zhang, C., Yang, L.-Y., Zhang, L.-L., Ji, W.-Q. & Wu, F.-Y. (2014). Formation of gabbronorites in the Purang ophiolite (SW Tibet) through melting of hydrothermally altered mantle along a detachment fault. *Lithos* **205**, 127–141.
- Liu, C.-Z., Chung, S.-L., Wu, F.-Y., Zhang, C., Xu, Y., Wang, J.-G., Chen, Y. & Guo, S. (2016a). Tethyan suturing in Southeast Asia: zircon U–Pb and Hf–O isotopic constraints from Myanmar ophiolites. *Geology* **44**, 311–314.
- Liu, T., Wu, F.-Y., Zhang, L.-L., Zhai, Q.-G., Liu, C.-Z., Ji, W.-B., Zhang, C. & Xu, Y. (2016b). Zircon U–Pb geochronological constraints on rapid exhumation of the mantle peridotite of the Xigaze ophiolite, southern Tibet. *Chemical Geology* **443**, 67–86.
- Liu, F., Dilek, Y., Xie, Y., Yang, J. & Lian, D. (2018a). Melt evolution of upper mantle peridotites and mafic dikes in the northern ophiolite belt of the western Yarlung Zangbo suture zone (southern Tibet). *Lithosphere* **10**, 109–132.
- Liu, T., Wu, F.-Y., Liu, C.-Z., Tribuzio, R., Ji, W.-B., Zhang, C., Xu, Y. & Zhang, W.-Q. (2018b). Variably evolved gabbroic intrusions within the Xigaze ophiolite (Tibet): new insights into the origin of ophiolite diversity. *Contributions to Mineralogy and Petrology* **173**, 91.
- Liu, T., Liu, C.-Z., Wu, F.-Y., Dick, H. J. B., Ji, W.-B., Zhang, C., Zhang, W.-Q., Zhang, Z.-Y. & Xu, Y. (2021). The Xigaze ophiolite: fossil ultraslow-spreading ocean lithosphere in the Tibetan plateau. *Journal of the Geological Society* **178**, 2020–2208.
- Liu, C.-Z., Wu, F.-Y., Liu, T., Zhang, C., Zhang, W.-Q., Zhang, Z.-Y., Zhang, Z., Wei, W. & Lin, Y.-Z. (2022). An origin of ultraslow spreading ridges for the Yarlung–Tsangpo ophiolites. *Fundamental Research* **2**, 74–83.
- Maffione, M., van Hinsbergen, D. J. J., Koornneef, L. M. T., Guilmette, C., Hodges, K., Borneman, N., Huang, W., Ding, L. & Kapp, P. (2015). Forearc hyperextension dismembered the south Tibetan ophiolites. *Geology* **43**, 475–478.
- Mahoney, J. J., Frei, R., Tejada, M., Mo, X., Leat, P. & Nägler, T. (1998). Tracing the Indian Ocean mantle domain through time: isotopic results from old west Indian, east Tethyan, and South Pacific seafloor. *Journal of Petrology* **39**, 1285–1306.
- Marchesi, C., Garrido, C. J., Godard, M., Belley, F. & Ferré, E. (2009). Migration and accumulation of ultra-depleted subduction-related melts in the Massif du Sud ophiolite (New Caledonia). *Chemical Geology* **266**, 171–186.
- Miller, C., Thöni, M., Frank, W., Schuster, R., Melcher, F., Meisel, T. & Zanetti, A. (2003). Geochemistry and tectonomagmatic affinity of the Yungbwa ophiolite, SW Tibet. *Lithos* **66**, 155–172.
- Morgan, Z., Liang, Y. & Kelemen, P. (2008). Significance of the concentration gradients associated with dunite bodies in the Josephine and Trinity ophiolites. *Geochemistry, Geophysics, Geosystems* **9**, Q07025.
- Morishita, T., Arai, S., Gervilla, F. & Green, D. H. (2003). Closed-system geochemical recycling of crustal materials in alpine-type peridotite. *Geochimica et Cosmochimica Acta* **67**, 303–310.
- Müntener, O., Kelemen, P. B. & Grove, T. L. (2001). The role of H<sub>2</sub>O during crystallization of primitive arc magmas under uppermost mantle conditions and genesis of igneous pyroxenites: an experimental study. *Contributions to Mineralogy and Petrology* **141**, 643–658.
- Nicolas, A., Girardeau, J., Marcoux, J., Dupre, B., Xibin, W., Yougong, C., Haixiang, Z. & Xuchang, X. (1981). The Xigaze ophiolite (Tibet): a peculiar oceanic lithosphere. *Nature* **294**, 414–417.
- Niu, X., Zhao, Z., XuanXue, M., DePaolo, D. J., Dong, G., Zhang, S., Zhu, D. & Guo, T. (2006). Elemental and Sr–Nd–Pb isotopic geochemistry for basic rocks from Decun–Angren ophiolites in Xigaze area, Tibet: implications for the characteristics of the Tethyan upper mantle domain. *Acta Petrologica Sinica*(12) **22**, 2875–2888.
- Palme, H. & O'Neill, H. S. C. (2014). 3.1 - Cosmochemical estimates of mantle composition. In: (Holland H. D. & Turekian K. K. (eds)) *Treatise on Geochemistry*, 2nd edn. Oxford: Elsevier, pp.1–39.
- Plank, T. (2014) The chemical composition of subducting sediments. In: (Holland H. D. & Turekian K. K. (eds)) *Treatise on Geochemistry*, vol. 3, 2nd edn. Oxford: Elsevier, pp.607–629.
- Python, M. & Ceuleneer, G. (2003). Nature and distribution of dykes and related melt migration structures in the mantle section of the Oman ophiolite. *Geochemistry, Geophysics, Geosystems*(7) **4**, 8612.
- Python, M., Ceuleneer, G. & Arai, S. (2008). Chromian spinels in mafic–ultramafic mantle dykes: evidence for a two-stage melt production during the evolution of the Oman ophiolite. *Lithos* **106**, 137–154.
- Rampone, E. & Borghini, G. (2008). Melt migration and intrusion in the Erro–Tobbio peridotites (Ligurian Alps, Italy): insights on magmatic processes in extending lithospheric mantle. *European Journal of Mineralogy* **20**, 573–585.
- Reagan, M. K., Ishizuka, O., Stern, R. J., Kelley, K. A., Ohara, Y., Blichert-Toft, J., Bloomer, S. H., Cash, J., Fryer, P., Hanan, B. B., Hickey-Vargas, R., Ishii, T., Kimura, J.-I., Peate, D. W., Rowe, M. C. & Woods, M. (2010). Fore-arc basalts and subduction initiation in the Izu–Bonin–Mariana system. *Geochemistry, Geophysics, Geosystems* **11**, Q03X12.
- Richards, A., Argles, T., Harris, N., Parrish, R., Ahmad, T., Darbyshire, F. & Draganits, E. (2005). Himalayan architecture constrained by isotopic tracers from clastic sediments. *Earth and Planetary Science Letters* **236**, 773–796.
- Roduit, N. (2008) JMicroVision: Image Analysis Toolbox for Measuring and Quantifying Components of High-Definition Images. Version 1.2.7. <http://www.jmicrovision.com>.
- Salters, V. J. M., Mallick, S., Hart, S. R., Langmuir, C. E. & Stracke, A. (2011). Domains of depleted mantle: new evidence from hafnium and neodymium isotopes. *Geochemistry, Geophysics, Geosystems* **12**, Q08001.
- Schiemenz, A., Liang, Y. & Parmentier, E. M. (2011). A high-order numerical study of reactive dissolution in an upwelling heterogeneous mantle I. Channelization, channel lithology and channel geometry. *Geophysical Journal International* **186**, 641–664.
- Sergeev, D. S., Dijkstra, A. H., Meisel, T., Brüggemann, G. & Sergeev, S. A. (2014). Traces of ancient mafic layers in the Tethys oceanic mantle. *Earth and Planetary Science Letters* **389**, 155–166.
- Seyler, M., Brunelli, D., Toplis, M. J. & Mével, C. (2011). Multi-scale chemical heterogeneities beneath the eastern southwest Indian ridge (52°E–68°E): trace element compositions of along-axis dredged peridotites. *Geochemistry, Geophysics, Geosystems* **12**, Q0AC15.
- Smith, P. M. & Asimow, P. D. (2005). Adibat\_1ph: a new public front-end to the MELTS, pMELTS, and pHMELTS models. *Geochemistry, Geophysics, Geosystems* **6**, Q02004.
- Söderlund, U., Patchett, P. J., Vervoort, J. D. & Isachsen, C. E. (2004). The <sup>176</sup>Lu decay constant determined by Lu–Hf and U–Pb isotope systematics of Precambrian mafic intrusions. *Earth and Planetary Science Letters* **219**, 311–324.
- Stracke, A., Bizimis, M. & Salters, V. J. (2003). Recycling oceanic crust: quantitative constraints. *Geochemistry, Geophysics, Geosystems*(3) **4**, 8003.

- Su, B.-X., Teng, F.-Z., Hu, Y., Shi, R.-D., Zhou, M.-F., Zhu, B., Liu, F., Gong, X.-H., Huang, Q.-S., Xiao, Y., Chen, C. & He, Y.-S. (2015). Iron and magnesium isotope fractionation in oceanic lithosphere and sub-arc mantle: perspectives from ophiolites. *Earth and Planetary Science Letters* **430**, 523–532.
- Suhr, G., Hellebrand, E., Snow, J. E., Seck, H. A. & Hofmann, A. W. (2003). Significance of large, refractory dunite bodies in the upper mantle of the Bay of Islands ophiolite. *Geochemistry, Geophysics, Geosystems* **4**, 2003.
- Sun, C. (2014). Trace element partitioning in mantle minerals with applications to subsolidus re-equilibration and thermobarometry. Ph.D. thesis. <https://bruknow.library.brown.edu/discovery/>.
- Sun, C. & Liang, Y. (2012). Distribution of REE between clinopyroxene and basaltic melt along a mantle adiabat: effects of major element composition, water, and temperature. *Contributions to Mineralogy and Petrology* **163**, 807–823.
- Sun, C. & Liang, Y. (2013). Distribution of REE and HFSE between low-Ca pyroxene and lunar picritic melts around multiple saturation points. *Geochimica et Cosmochimica Acta* **119**, 340–358.
- Sun, S. & McDonough, W. F. (1989). Chemical and isotopic systematics of oceanic basalts: implications for mantle composition and processes. *Geological Society, London, Special Publications* **42**, 313–345.
- Tamura, A. & Arai, S. (2006). Harzburgite–dunite–orthopyroxenite suite as a record of supra-subduction zone setting for the Oman ophiolite mantle. *Lithos* **90**, 43–56.
- Tilhac, R., Ceuleneer, G., Griffin, W. L., O'Reilly, S. Y., Pearson, N. J., Benoit, M., Henry, H., Girardeau, J. & Grégoire, M. (2016). Primitive arc magmatism and delamination: petrology and geochemistry of pyroxenites from the Cabo Ortegal complex, Spain. *Journal of Petrology* **57**, 1921–1954.
- Varfalvy, V., Hébert, R. & Bedard, J. H. (1996). Interactions between melt and upper-mantle peridotites in the north arm mountain massif, Bay of Islands ophiolite, Newfoundland, Canada: implications for the genesis of boninitic and related magmas. *Chemical Geology* **129**, 71–90.
- Villiger, S., Müntener, O. & Ulmer, P. (2007). Crystallization pressures of mid-ocean ridge basalts derived from major element variations of glasses from equilibrium and fractional crystallization experiments. *Journal of Geophysical Research: Solid Earth* **112**, B01202.
- Wang, C., Ding, L., Zhang, L.-Y., Kapp, P., Pullen, A. & Yue, Y.-H. (2016a). Petrogenesis of middle–late Triassic volcanic rocks from the Gangdese belt, southern Lhasa terrane: implications for early subduction of Neo-Tethyan oceanic lithosphere. *Lithos* **262**, 320–333.
- Wang, C., Liang, Y., Dygert, N. & Xu, W. (2016b). Formation of orthopyroxenite by reaction between peridotite and hydrous basaltic melt: an experimental study. *Contributions to Mineralogy and Petrology* **171**, 77.
- Wang, J.-G., Hu, X., Garzanti, E., An, W. & Liu, X.-C. (2017). The birth of the Xigaze forearc basin in southern Tibet. *Earth and Planetary Science Letters* **465**, 38–47.
- Warren, J. M. (2016). Global variations in abyssal peridotite compositions. *Lithos* **248–251**, 193–219.
- Warren, J. M., Shimizu, N., Sakaguchi, C., Dick, H. J. B. & Nakamura, E. (2009). An assessment of upper mantle heterogeneity based on abyssal peridotite isotopic compositions. *Journal of Geophysical Research: Solid Earth* **114**, B12203.
- Weaver, S. L., Wallace, P. J. & Johnston, A. D. (2011). A comparative study of continental vs. intraoceanic arc mantle melting: experimentally determined phase relations of hydrous primitive melts. *Earth and Planetary Science Letters* **308**, 97–106.
- Wei, Z., Xia, B., Zhang, Y., Wang, R., Yang, Z. & Wei, D. (2006). SHRIMP zircon dating of diabase in the Xiugugabu ophiolite in Tibet and its geological implications. *Geotectonica et Metallogenia* **30**, 93–97.
- Woelki, D., Regelous, M., Haase, K. M., Romer, R. H. W. & Beier, C. (2018). Petrogenesis of boninitic lavas from the Troodos ophiolite, and comparison with Izu–Bonin–Mariana fore-arc crust. *Earth and Planetary Science Letters* **498**, 203–214.
- Woodland, S., Pearson, D. & Thirlwall, M. (2002). A platinum group element and Re–Os isotope investigation of siderophile element recycling in subduction zones: comparison of Grenada, Lesser Antilles arc, and the Izu–Bonin arc. *Journal of Petrology* **43**, 171–198.
- Workman, R. K. & Hart, S. R. (2005). Major and trace element composition of the depleted MORB mantle (DMM). *Earth and Planetary Science Letters* **231**, 53–72.
- Wu, F.-Y., Ji, W.-Q., Liu, C.-Z. & Chung, S.-L. (2010). Detrital zircon U–Pb and Hf isotopic data from the Xigaze fore-arc basin: constraints on Transhimalayan magmatic evolution in southern Tibet. *Chemical Geology* **271**, 13–25.
- Xiong, Q., Zheng, J. P., Griffin, W. L., O'Reilly, S. Y. & Pearson, N. J. (2014). Pyroxenite dykes in orogenic peridotite from north Qaidam (NE Tibet, China) track metasomatism and segregation in the mantle wedge. *Journal of Petrology* **55**, 2347–2376.
- Xiong, Q., Griffin, W. L., Zheng, J.-P., O'Reilly, S. Y., Pearson, N. J., Xu, B. & Belousova, E. A. (2016). Southward trench migration at ~130–120 Ma caused accretion of the Neo-Tethyan forearc lithosphere in Tibetan ophiolites. *Earth and Planetary Science Letters* **438**, 57–65.
- Xiong, F., Yang, J., Robinson, P. T., Xu, X., Liu, Z., Zhou, W., Feng, G., Xu, J., Li, J. & Niu, X. (2017a). High-Al and high-Cr podiform chromitites from the western Yarlung–Zangbo suture zone, Tibet: implications from mineralogy and geochemistry of chromian spinel, and platinum-group elements. *Ore Geology Reviews* **80**, 1020–1041.
- Xiong, Q., Griffin, W. L., Zheng, J. P., Pearson, N. J. & O'Reilly, S. Y. (2017b). Two-layered oceanic lithospheric mantle in a Tibetan ophiolite produced by episodic subduction of Tethyan slabs. *Geochemistry, Geophysics, Geosystems* **18**, 1189–1213.
- Xiong, Q., Henry, H., Griffin, W. L., Zheng, J.-P., Satsukawa, T., Pearson, N. J. & O'Reilly, S. Y. (2017c). High- and low-Cr chromitite and dunite in a Tibetan ophiolite: evolution from mature subduction system to incipient forearc in the Neo-Tethyan Ocean. *Contributions to Mineralogy and Petrology* **172**, 45.
- Xu, J.-F. & Castillo, P. R. (2004). Geochemical and Nd–Pb isotopic characteristics of the Tethyan asthenosphere: implications for the origin of the Indian Ocean mantle domain. *Tectonophysics* **393**, 9–27.
- Xu, D.-M., Huang, G. G. & Li, Y.-J. (2008). Sm–Nd ages and Nd–Sr–Pb isotope signatures of the Xiugugabu ophiolite, southwestern Tibet. *Geology in China* **35**, 429–435.
- Yang, J.-H., Chung, S.-L., Wilde, S. A., Wu, F.-Y., Chu, M.-F., Lo, C.-H. & Fan, H.-R. (2005). Petrogenesis of post-orogenic syenites in the Sulu Orogenic Belt, East China: geochronological, geochemical and Nd–Sr isotopic evidence. *Chemical Geology* **214**, 99–125.
- Yao, L., Sun, C. & Liang, Y. (2012). A parameterized model for REE distribution between low-Ca pyroxene and basaltic melts with applications to REE partitioning in low-Ca pyroxene along a mantle adiabat and during pyroxenite-derived melt and peridotite interaction. *Contributions to Mineralogy and Petrology* **164**, 261–280.

- Yin, A. & Harrison, T. M. (2000). Geologic evolution of the Himalayan–Tibetan orogen. *Annual Review of Earth and Planetary Sciences* **28**, 211–280.
- Yu, S. Y., Xu, Y. G., Ma, J. L., Zheng, Y. F., Kuang, Y. S., Hong, L. B., Ge, W. C. & Tong, L. X. (2010). Remnants of oceanic lower crust in the subcontinental lithospheric mantle: trace element and Sr–Nd–O isotope evidence from aluminous garnet pyroxenite xenoliths from Jiaohe, Northeast China. *Earth and Planetary Science Letters* **297**, 413–422.
- Zhang, C. (2017). New insights into the genesis of Yarlung–Tsangbo ophiolite, southern Tibet: near-margin dying ridge and noncon-sanguineous crust-mantle. Ph.D. thesis (in Chinese with English abstract). 1–210. <http://dpaper.las.ac.cn/>.
- Zhang, S. Q., Mahoney, J. J., Mo, X. X., Ghazi, A. M., Milani, L., Crawford, A. J., Guo, T. Y. & Zhao, Z. D. (2005). Evidence for a widespread Tethyan upper mantle with Indian Ocean-type isotopic characteristics. *Journal of Petrology* **46**, 829–858.
- Zhang, X., Ganguly, J. & Ito, M. (2009). Ca–Mg diffusion in diopside: tracer and chemical inter-diffusion coefficients. *Contributions to Mineralogy and Petrology* **159**, 175.
- Zhang, L.-L., Liu, C.-Z., Wu, F.-Y., Ji, W.-Q. & Wang, J.-G. (2014). Zedong terrane revisited: an intra-oceanic arc within Neo-Tethys or a part of the Asian active continental margin? *Journal of Asian Earth Sciences* **80**, 34–55.
- Zhang, C., Liu, C.-Z., Wu, F.-Y., Zhang, L.-L. & Ji, W.-Q. (2016a). Geochemistry and geochronology of mafic rocks from the Luobusa ophiolite, South Tibet. *Lithos* **245**, 93–108.
- Zhang, L.-L., Liu, C.-Z., Wu, F.-Y., Zhang, C., Ji, W.-Q. & Wang, J.-G. (2016b). Sr–Nd–Hf isotopes of the intrusive rocks in the creta-ceous Xigaze ophiolite, southern Tibet: constraints on its formation setting. *Lithos* **258–259**, 133–148.
- Zhang, C., Liu, C.-Z., Xu, Y., Ji, W.-B., Wang, J.-M., Wu, F.-Y., Liu, T., Zhang, Z.-Y. & Zhang, W.-Q. (2019). Subduction re-initiation at dying ridge of Neo-Tethys: insights from mafic and metamafic rocks in Lhaze ophiolitic mélangé, Yarlung–Tsangbo suture zone. *Earth and Planetary Science Letters* **523**, 115707.
- Zhang, C., Liu, C.-Z., Ji, W.-B., Liu, T. & Wu, F.-Y. (2020a). Heterogeneous sub-ridge mantle of the Neo-Tethys: constraints from Re–Os isotope and HSE compositions of the Xigaze ophiolites. *Lithos* **378–379**, 105819.
- Zhang, C., Liu, C.-Z., Liu, T. & Wu, F.-Y. (2020b). Evolution of mantle peridotites from the Luobusa ophiolite in the Tibetan plateau: Sr–Nd–Hf–Os isotope constraints. *Lithos* **362–363**, 105477.
- Zhong, Y., Liu, W.-L., Tang, G.-J., Liu, N.-N., Liu, H.-F., Zeng, Q.-G. & Xia, B. (2019). Origin of Mesozoic ophiolitic mélanges in the western Yarlung Zangbo suture zone, SW Tibet. *Gondwana Research* **76**, 204–223.